

Mimetic DBI Inflation in Confrontation with Planck2018 data

Kourosh Nozari^{a,b,1} and Narges Rashidi^{a,2}

^aDepartment of Physics, Faculty of Basic Sciences, University of Mazandaran,
P. O. Box 47416-95447, Babolsar, IRAN

^b Research Institute for Astronomy and Astrophysics of Maragha (RIAAM),
P. O. Box 55134-441, Maragha, Iran

Abstract

We study mimetic gravity in the presence of a DBI-like term which is a non-canonical setup of the scalar field's derivatives. We consider two general cases with varying and constant sound speeds and construct the potentials for both the DBI and Mimetic DBI models. By considering the power-law scale factor as $a = a_0 t^n$, we seek for the observational viability of these models. We show that, the Mimetic DBI model in some ranges of the parameters space is free of ghost and gradient instabilities. By studying $r - n_s$ and $\alpha_s - n_s$ behavior in confrontation with Planck2018 data, we find some constraints on the model's parameters. We show that for the case with varying sound speed, although power-law DBI inflation is not consistent with Planck2018 TT, TE, EE+low E+lensing data, but the Mimetic DBI inflation is consistent with Planck2018 TT, TE, EE+low E+lensing data at 95% CL, in some ranges of the model's parameters space as $40 \leq n \leq 55$ where the model is instabilities-free in these ranges of parameters too. For the constant sound speed, by adopting some sample values of c_s , we study both DBI and Mimetic DBI model numerically and find $n \sim 10^2$ for DBI model and $n \sim 10$ for Mimetic DBI model. We also compare the results with Planck2018 TT, TE, EE+low E+lensing+BK14+BAO data and see that the DBI and Mimetic DBI model with varying sound speed are ruled out with these joint data. However, these models with constant sound speed are consistent with Planck2018 TT, TE, EE+low E+lensing+BK14+BAO data with $n \sim 10^2$ for DBI model and $n \sim 10$ for Mimetic DBI model. In this case, we find some tighter constraints on the corresponding sound speed.

PACS: 98.80.Bp, 98.80.Cq, 98.80.Es

Key Words: Cosmological Inflation, DBI Model, Mimetic Gravity, Observational Constraints

¹knozari@umz.ac.ir

²n.rashidi@umz.ac.ir

1 Introduction

In 2013, Chamseddine and Mukhanov have proposed a new approach to General Relativity, respecting the conformal symmetry as an internal degree of freedom [1]. In their proposal, the authors have introduced a model in which the physical metric is written in terms of an auxiliary metric and a scalar field as follows

$$g_{\mu\nu} = -\tilde{g}^{\alpha\beta} \phi_{,\alpha} \phi_{,\beta} \tilde{g}_{\mu\nu}. \quad (1)$$

The scalar field ϕ is a free and non-dynamical field which encodes the conformal mode of the gravity. Considering the definition given in equation (1), we see that the physical metric ($g_{\mu\nu}$) remains invariant with respect to the Weyl transformation of the auxiliary metric ($\tilde{g}_{\mu\nu}$). Note that, the definition (1) leads to the following constraint on the scalar field [1]

$$g^{\mu\nu} \phi_{,\mu} \phi_{,\nu} = -1, \quad (2)$$

In Ref. [1], the action consists of the Einstein-Hilbert term and the contribution of the matter coupled to $g_{\mu\nu}$. The Einstein's field equations in this model consist of an extra term which corresponds to the mimetic field. This extra term is considered as a source of the dark matter. Actually, in the energy density, there is a term corresponding to a^{-3} which “mimics” the dark matter. In Ref. [2], by using the Lagrange multipliers in the action, the author has introduced another mathematical approach to explore the mimetic matter scenario (see also [3]). The ghost free models of the mimetic dark matter theory have been discussed in [4]. The lagrange multiplier approach has been followed in [5] where the authors have considered the Lagrange multiplier in the action and also a potential for the mimetic field. The authors in this paper have shown that by adopting the appropriate potentials, it is possible to consider the mimetic field as quintessence, phantom or inflaton fields. Other extensions of the mimetic model, such as the non-minimal mimetic model [6, 7], braneworld mimetic model [8] and mimetic gravity in the spirit of $f(R)$ theories [9, 10, 11], mimetic $f(G)$ gravity [12], mimetic Horndeski gravity [13, 14], mimetic Galileon gravity [15], unimodular mimetic $f(R)$ gravity [16] and mimetic Born-Infeld theory [17, 18] have been studied.

In the ordinary mimetic model, where even a potential is included, the sound speed of the perturbations is vanishing and the perturbations behave like a dust [5]. In this regard, adding higher derivative terms such as $\gamma \square \phi$ (where γ is a constant) leads to a non-zero sound speed of the perturbations [5]. By appropriate choosing of γ , the mimetic model with $\gamma \square \phi$ term can be ghost free, however, it still suffers from the gradient instability [19]. The authors of [20] have shown that by considering the direct couplings of the higher derivatives of the mimetic field to the curvature of the space-time, it is possible to overcome such instabilities in some ranges of the parameters space. For more papers on the (in)stability issue see [21, 22, 23, 24, 25, 26, 27, 28, 29, 30, 30, 31, 32].

In this paper, instead of including the higher order derivatives of the scalar field, we consider a non-canonical setup of the scalar field's derivatives. DBI [33, 34, 35, 36] and tachyon [37, 38, 39, 40, 41, 42] fields are examples of the non-canonical scalar fields. We add a DBI like term, $f^{-1}(\phi) \sqrt{1 - f \dot{\phi}^2}$, in the action of the simple mimetic model with potential. Here, the field ϕ in DBI term is the mimetic scalar field. In the string based DBI (Dirac-Born-Infeld) model, the scalar field is characterized by the radial position of a $D3$ brane [33, 35]. This brane moves in a “throat” region of a warped compactified space while there is a speed limit on its motion [33]. This scalar field can be considered as inflaton with non-canonical kinetic term. In the DBI inflation model

the sound speed of the primordial perturbation is different from unity (considering c , the speed of light, to be unity) which can lead to large non-Gaussianity [35, 36, 43]. For more work on the DBI inflation see [44, 45, 46, 47, 48, 49, 50, 51, 52, 53, 54, 55]. However, in this paper we assume the field in the DBI term to be the mimetic scalar field. We are going to explore the cosmological dynamics of the mimetic model in the presence of the DBI-like term. We wonder, by adding this term, if the the mimetic model would be stable- meaning that, it would be free of the gradient and ghost instabilities or not. We also seek for the observational viability of the model. To this end, we study the Mimetic DBI (from now on, MDBI) model with power-law scale factor [56, 57, 58, 59, 60, 45]. In this regard we consider a mimetic model with DBI-like term and potential, and also use the lagrange multiplier in the action. We follow Refs. [61, 62] to find the appropriate potential and lagrange multiplier corresponding to the power-law scale factor, and then check the observational viability of the model.

This paper is organized as follows: In section 2, we consider the case with varying sound speed. In subsection 2.1, we consider an ordinary DBI model and obtain the main background equations of the model. By introducing the slow-roll parameters and the sound speed of the model, we obtain the main perturbation parameters like as the tensor-to-scalar ratio, scalar spectral index and its running. We also construct the potential of the model in terms of the Hubble parameter and its derivatives. In subsection 2.2 we consider a power-law scale factor and recast the slow-roll parameters (and therefore the perturbation parameters) of the DBI model in terms of the new parameters of the introduced scale factor. Given that, for the DBI model we obtain two forms of potential and we analyze the perturbations parameters for both cases. As we shall see, the DBI model that we study here, is not observationally viable. But this not the end of the road. In section 2.3, we introduce the Mimetic DBI inflation. In this section, by using the Lagrange multiplier, we enter the mimetic constraint. In this section also, we obtain the background equations of the model. By using the Friedmann equations, we obtain the Lagrange multiplier and the potential in terms of the Hubble parameter and its derivatives. We also find the slow-roll parameters in our MDBI model which differs from the ones in usual DBI model. In section 2.4, we study the power-law MDBI model. We show that, by adding a DBI-like term in the action of the mimetic model with potential term, and by considering a power-law scale factor, the mimetic model would be free of gradient instability in some ranges of the model's parameters space. We show that the model is free of ghost instability in some ranges of the model's parameters space which mach with the ranges leading to the gradient instability free MDBI model. We also explore the perturbation parameters numerically. The interesting point is that, $r - n_s$ and $\alpha_s - n_s$ are consistent with observational data in ranges of the model's parameters space where the MDBI model is stable. Although these ranges lead to small non-Gaussianity, but it is consistent with observational data. We use the constraints obtained from $r - n_s$ and $\alpha_s - n_s$ to find the viable values of the non-Gaussianity. In section 3 we use the constraint on the nonlinearity parameter (in the non-Gaussianity) and constraint on the sound speed to explore other features of the model. In this regard, we consider constant sound speed and adopt some observationally viable values of this quantity. By using the adopted values of the sound speed, we study $r - n_s$ and $\alpha - n_s$ for DBI model in subsection 3.1 and MDBI model in subsection 3.2 and find some constraints on the model's parameters. In section 4, we consider the B-mode polarization and use the BICEP2/Keck Array 2014 and Planck2018 joint data to explore the models. As another important result, the DBI and MDBI models with power-law scale factor and varying sound speed are ruled out by the BICEP2/Keck Array 2014 and Planck2018 joint data. Therefore, in section 4 we only perform numerical analysis on these models with constant

sound speed and find some constraints on the model. In section 5, we present the summary and conclusion.

2 Varying Sound speed

In this section, we consider the case with varying sound speed where the sound speed is expressed in terms of the model's parameters. In this case, by using the observational viability of n_s , r and α_s , we obtain some constraints on n (remember that $a = a_0 t^n$). Then, by using the constraints on n , we obtain the observational viable values of c_s and the prediction of the model for non-Gaussian features.

2.1 DBI Model

We consider the following action for the DBI model

$$S = \int d^4x \sqrt{-g} \left[\frac{1}{2\kappa^2} R - f^{-1}(\phi) \sqrt{1 - 2f(\phi)X} - V(\phi) \right], \quad (3)$$

where, R is the Ricci scalar, $V(\phi)$ is the potential of the field, $f^{-1}(\phi)$ is the inverse brane tension, related to the geometry of the throat of the compact manifold passed by the D3-brane and $X = -\frac{1}{2}\partial_\nu\phi\partial^\nu\phi$.

Variation of the action (3) with respect to the metric leads to the following Einstein's field equations

$$G_{\mu\nu} = \kappa^2 \left[-g_{\mu\nu} f^{-1} \sqrt{1 + f g^{\mu\nu} \partial_\mu\phi \partial_\nu\phi} - g_{\mu\nu} V + \partial_\mu\phi \partial_\nu\phi \left(1 + f g^{\mu\nu} \partial_\mu\phi \partial_\nu\phi \right)^{-\frac{1}{2}} \right], \quad (4)$$

which by considering the flat FRW metric

$$ds^2 = -dt^2 + a^2(t) \delta_{ij} dx^i dx^j, \quad (5)$$

lead to the following Friedmann equations

$$3H^2 = \kappa^2 \left[\frac{f^{-1}}{\sqrt{1 - f\dot{\phi}^2}} + V \right], \quad (6)$$

$$2\dot{H} + 3H^2 = \kappa^2 \left[f^{-1} \sqrt{1 - f\dot{\phi}^2} + V \right]. \quad (7)$$

Variation of the action (3) with respect to ϕ gives the equation of motion as [52]

$$\frac{\ddot{\phi}}{(1 - f\dot{\phi}^2)^{\frac{3}{2}}} + \frac{3H\dot{\phi}}{(1 - f\dot{\phi}^2)^{\frac{1}{2}}} + V' = -\frac{f'}{f^2} \left[\frac{3f\dot{\phi}^2 - 2}{2(1 - f\dot{\phi}^2)^{\frac{1}{2}}} \right]. \quad (8)$$

In this paper we are going to study the cosmic inflationary phase in this setup. To have the inflation phase, the slow-roll parameters should be much smaller than unity. These parameters are defined as

$$\epsilon \equiv -\frac{\dot{H}}{H^2}, \quad \eta = -\frac{1}{H} \frac{\ddot{H}}{\dot{H}}, \quad s = \frac{1}{H} \frac{d \ln c_s}{dt}, \quad (9)$$

where c_s is the sound speed of the perturbations. To have inflation phase, the constraints $f\dot{\phi}^2 \ll 1$ and $\ddot{\phi} \ll 3H\dot{\phi}$ should be satisfied.

In this model, the square of sound speed which is defined as $c_s^2 = \frac{P_{,X}}{\rho_{,X}}$ (where the subscript “, X ” shows derivative with respect to X), is given by

$$c_s^2 = 1 - f\dot{\phi}^2. \quad (10)$$

The sound speed should satisfy two constraints as follows [63, 64]. To avoid the appearance of gradient instabilities, the square of the sound speed of the perturbation should be positive, that is, $c_s^2 > 0$. Also, by considering the causality requirement, the maximum value of the sound speed should be equal to the value of the local speed of light- that means $c_s \leq c$, where c is the local speed of light. By adopting $c \equiv 1$, these constraints imply that $0 < c_s^2 \leq c^2$.

In this paper, we are going to seek for the observational viability of the model by comparing the results of our model with the Planck2018 observational data [65, 66] and constraining the perturbation parameters. To constraint the perturbation parameters, Planck collaboration has used this fact that the two-point correlations of the CMB anisotropies are described by the angular power spectra C_l^{TT} , C_l^{TE} , C_l^{EE} and C_l^{BB} (l is the multipole moment number), under the assumption of statistical isotropy [67, 68, 69, 70, 71]. Via the transfer functions $\Delta_{l,A}^s$ and $\Delta_{l,A}^T$ (whic are generally computed by using the Boltzmann codes such as CMBFAST [72] or CAMB [73]), the Planck collaboration has related the CMB angular power spectra to the scalar and tensor primordial power spectra. If we consider $a, b = T, E, B$, the contributions from scalar and tensor perturbations in the CMB angular power spectra are given by [74]

$$C_l^{ab,s} = \int_0^\infty \frac{dk}{k} \Delta_{l,a}^s(k) \Delta_{l,b}^s(k) \mathcal{A}_s(k), \quad (11)$$

$$C_l^{ab,T} = \int_0^\infty \frac{dk}{k} \Delta_{l,a}^T(k) \Delta_{l,b}^T(k) \mathcal{A}_T(k). \quad (12)$$

The linear transformations encoded in $\Delta_{l,B}^i(k)$ (with $i = s, T$) are corresponding to the physics of the late time and the primordial power spectra $\mathcal{A}_i(k)$ are identified by the physics of the primordial universe [74]. To explore the transfer functions, and seek for the CMB anisotropies, the Planck team has adopted the Λ CDM model as the one governing on the late time background dynamics of the universe. Also, to compare the perturbations parameters with data, they expand the scalar and tensor power spectra as [66, 74]³

$$\mathcal{A}_s(k) = A_s \left(\frac{k}{k_*} \right)^{n_s - 1 + \frac{1}{2} \frac{dn_s}{d \ln k} \ln \left(\frac{k}{k_*} \right) + \frac{1}{6} \frac{d^2 n_s}{d \ln k^2} \ln \left(\frac{k}{k_*} \right)^2 + \dots}, \quad (13)$$

³Actually, the Planck collaboration has adopted three procedures to compare the inflationary parameters with data. One procedure is corresponding to the parameterization of the primordial spectra as equations (13) and (14). Another one is corresponding to the dependence of the slow-roll power spectra on the Hubble flow-functions. The third procedure is numerical and uses the numerical codes like the CLASS [75, 76] and ModeCode [77, 79]. For more details see [74].

$$\mathcal{A}_T(k) = A_T \left(\frac{k}{k_*} \right)^{n_T + \frac{1}{2} \frac{dn_T}{d \ln k} \ln \left(\frac{k}{k_*} \right) + \dots}, \quad (14)$$

which are model independent and where, A_i is the amplitude of the scalar ($i = s$) or tensor ($i = T$) perturbations. Also, $\frac{dn_i}{d \ln k}$ is the the running of the scalar ($i = s$) or tensor ($i = T$) spectral index and $\frac{d^2 n_s}{d \ln k^2}$ is the running of the running of the scalar spectral index. Using the power spectra, it is possible to find the ratio of the tensor to scalar amplitudes of the perturbations as

$$r = \frac{\mathcal{A}_T(k_*)}{\mathcal{A}_s(k_*)}, \quad (15)$$

which is an important perturbation parameter. In this paper, we consider the constraints on the perturbation parameters obtained by Planck2018 team, based on the Λ CDM+ $r + \frac{dn_s}{d \ln k}$ model which supports quasi-de Sitter expansion during inflation epoch. In the Λ CDM+ $r + \frac{dn_s}{d \ln k}$ model, the amplitude and the scale dependence of the tensor perturbations, the amplitude and the scale dependence of the scalar perturbations and the scale dependence of the scalar spectral index are taken into account. From the Planck2018 TT, TE, EE+ low EB+ lensing data, the constraint on the scalar spectral index in Λ CDM+ $r + \frac{dn_s}{d \ln k}$ model is as $n_s = 0.9647 \pm 0.0044$, the constraint on the tensor-to-scalar ratio is as $r < 0.16$ and the constraint on the running of the scalar spectral index is as $\frac{dn_s}{d \ln k} = -0.0085 \pm 0.0073$, which are calculated at pivot scale $k_* = 0.002 Mpc^{-1}$ [66]. Note that, Planck2018 team has obtained some constraints based on Λ CDM+ r model too ($n_s = 0.9659 \pm 0.0041$ and $r < 0.10$ from Planck2018 TT, TE, EE+ low EB+ lensing), however, here we focus on the results of Λ CDM+ $r + \frac{dn_s}{d \ln k}$ model [66].

Now, we should obtain the perturbation parameters in the DBI model. Following the Planck collaboration assumption, we assume the late-time background dynamics is governed by Λ CDM model and the running of the spectral index is taken into account. The scale dependence of the scalar spectral index is identified by

$$n_s - 1 = \left. \frac{d \ln \mathcal{A}_s}{d \ln k} \right|_{c_s k = aH} \quad (16)$$

In this equation, the subscript $c_s k = aH$ means that the scalar spectral index is calculated at the time of sound horizon exit of the physical scales. Note that, although we consider the running of the scalar spectral index, but since the inflationary parameters are calculated at pivot scale $k = k_*$, the running term doesn't appear in definition (16). The amplitude of the scalar spectral index, which Planck2018 TT, TE, EE+ low EB+ lensing data gives its value as $\mathcal{A}_s \simeq 2.0989 \times 10^{-9}$ [66], is given by (see [52] for instance)

$$\mathcal{A}_s = \frac{H^2}{8\pi^2 \mathcal{W}_s c_s^3}, \quad (17)$$

where

$$\mathcal{W}_s = \frac{\dot{\phi}^2}{2H^2 (1 - f \dot{\phi}^2)^{3/2}}. \quad (18)$$

To avoid the ghost instability, \mathcal{W}_s should be positive.

We can write the scalar spectral index, in terms of the slow-roll parameters, as follows

$$n_s = 1 - 6\epsilon + 2\eta - s. \quad (19)$$

As we have mentioned earlier, the Planck2018 TT, TE, EE+low EB+lensing data gives the value of the scalar spectral index as $n_s = 0.9647 \pm 0.0044$ (in the Λ CDM+ $r + \frac{dn_s}{d\ln k}$ model) [66]. Another important parameter is the running of the scalar spectral index which is given by

$$\alpha_s = 8\epsilon\eta - 12\epsilon^2 - 2\zeta + 2\eta^2 - \frac{1}{H}\dot{s}, \quad (20)$$

where

$$\zeta = \frac{\ddot{H}}{H^2\dot{H}}. \quad (21)$$

The value of the running of the scalar spectral index, from Planck2018 TT, TE, EE + low EB+lensing data is as $\alpha_s = -0.0085 \pm 0.0073$ [66].

From equation (14) we see that the tensor spectral index is defined as follows

$$n_T = \left. \frac{d \ln \mathcal{A}_T}{d \ln k} \right|_{k=aH}, \quad (22)$$

where, the subscript $k = aH$ means that the tensor spectral index is calculated at Hubble horizon crossing of the physical scale. In definition (22), \mathcal{A}_T , the amplitude of the tensor perturbations, is given by

$$\mathcal{A}_T = \frac{2\kappa^2 H^2}{\pi^2}. \quad (23)$$

Now, we have the tensor spectral index as

$$n_T = -2\epsilon. \quad (24)$$

Considering that there is no detection of a non-zero tensor amplitude by current data [66], when r is very small (actually enough close to zero), any values of the tensor perturbations is viable in essence [66]. By relaxing the inflationary consistency relation and considering Planck2018 TT, TE, EE+ low E +lensing+ BK14+ LIGO & Virgo2016 data the Planck team have obtained the constraint on the tensor part as $-0.62 < n_T < 0.53$. However, there is no exact value of n_t . In Ref. [80], one can see the different delensing techniques and their ability to constraint the tensor spectral index.

By using equations (15) and (24) we obtain the tensor-to-scalar ratio as follows

$$r = 16 c_s \epsilon, \quad (25)$$

or

$$r = -8 c_s n_T. \quad (26)$$

Equation (26) is named the consistency relation. Note that in the simple single filed inflation with a canonical scalar field we have $c_s^2 = 1$ and therefore $r = 16\epsilon$. However, in the non canonical

DBI field the tensor-to-scalar ratio is given by Eq. (26). In some extended models, there is some additional terms in consistency relation. In other words, in those cases, the consistency relation is modified [40, 41, 81, 82, 83]. As we said, the constraint on the tensor-to-scalar ratio, from Planck2018 TT, TE, EE+ lowEB + lensing data, is as $r < 0.16$ [66].

Now, following Refs. [61, 62], we use the Friedmann equations to obtain the potential in terms of the Hubble parameter and its derivatives. First of all, we adopt $f^{-1}(\phi) = V(\phi)$. Then, we introduce a new scalar field φ which is identified by the number of e-folds N and parameterizes the scalar field ϕ as $\phi = \phi(\varphi)$. By using these points, equation (7) gives the following expression for the potential

$$V_{\pm} = -\frac{12H^2(N)H'(N)}{\kappa^2 \left(\pm\sqrt{3}\sqrt{H(N)}\sqrt{3H(N)+8H'(N)} + 3H(N) - 4H'(N) \right)}, \quad (27)$$

where a prime shows a derivative of the parameter with respect to N . We also find the following expressions for the slow-roll parameters in terms of the Hubble parameter and its derivatives

$$\epsilon_{\pm} = \frac{\left(H^3 H'' + H^2 H'^2 + \frac{4}{3} H^2 H' H'' + 4 H H'^3 \pm \frac{1}{\sqrt{3}} e H^{\frac{5}{2}} H'' \pm \frac{1}{\sqrt{3}} e H^{\frac{3}{2}} H'^2 \mp \frac{8}{3\sqrt{3}} e H'^3 \sqrt{H} \right)^2}{-\frac{4}{27} H^2 \left(\sqrt{3} e \sqrt{H} + 3H - 4H' \right)^2 H'^3 (3H + 8H')}, \quad (28)$$

where, $e \equiv \sqrt{H + 8H'}$ and $H \equiv H(N)$.

$$\eta_{\pm} = -\left\{ \frac{1}{4V_{\pm}^2} \left[-\frac{\kappa^2}{2} \left(1 - \frac{HH''}{H'^2} \right) V'_{\pm} - \frac{\kappa^2 H V''_{\pm}}{H'} - 2 \left(\frac{\kappa^2}{4} \left(1 - \frac{HH''}{H'^2} \right) \frac{V'_{\pm}}{V_{\pm}^2} - \frac{\kappa^2 H}{2 H'} \left(2 \frac{V_{\pm}^{\prime 2}}{V_{\pm}^3} - \frac{V''_{\pm}}{V_{\pm}^2} \right) V_{\pm}^2 \right] + \frac{1}{2} \frac{V_{\pm}^{\prime 2} \kappa^2 H}{H' V_{\pm}^2} \right\} \kappa^{-2}, \quad (29)$$

$$s = \frac{1}{2H} \left\{ -2 \frac{V'_{\pm} H^2 H'}{V_{\pm}^2 \kappa^2} - 2 \frac{H^2}{V_{\pm}} \left[-\left(\frac{H''}{H} - \frac{H'^2}{H^2} \right) \frac{\kappa^{-2} H}{\sqrt{-\frac{2H'}{\kappa^2 H}}} + \frac{H'}{\sqrt{-\frac{\kappa^2 H}{2H'}}} \right] \frac{1}{\sqrt{-\frac{\kappa^2 H}{2H'}}} \right\} \left(1 + 2 \frac{HH'}{V_{\pm} \kappa^2} \right)^{-1}. \quad (30)$$

Now, the perturbation parameters n_s and r can be expressed in terms of the Hubble parameter and its derivatives. By adopting some functions for the Hubble parameter, corresponding to some inflation model, we can analyze the observable parameters numerically.

Note that the tensor-to-scalar ratio is corresponding to the sound speed. This parameter is related to the other important property in the inflationary models, named “non-Gaussianity”. This property which is generated during the inflation era, can be used to test the observational viability of the inflation models. The Gaussian perturbations are characterized by two-point correlation. However, the additional statistical information corresponding to the non-Gaussian distribution can

be obtained from three and higher order correlations. The 3-point correlation in the interaction picture is defined as [84]

$$\langle \Phi(\mathbf{k}_1) \Phi(\mathbf{k}_2) \Phi(\mathbf{k}_3) \rangle = (2\pi)^7 \delta^3(\mathbf{k}_1 + \mathbf{k}_2 + \mathbf{k}_3) \mathcal{B}_\Phi(k_1, k_2, k_3), \quad (31)$$

where the potential Φ , which is equivalent to the Bardeen gravitational potential, is defined as $\Phi = \frac{3}{5}\xi$ with ξ to be the co-moving curvature perturbation. As we see from equation (31), the bispectrum \mathcal{B}_Φ depends on the three momenta \mathbf{k}_1 , \mathbf{k}_2 and \mathbf{k}_3 . By considering the translational and rotational invariance and depending on the amount of momenta, we are faced with different shapes of the non-Gaussianity with different corresponding amplitudes. In studying the non-Gaussian feature of the perturbation using the three-point correlation function, the so-called “nonlinearity parameter” measuring the amplitude of the non-Gaussianity of the primordial perturbations, is an important parameter which is related to the sound speed (see [35, 36]). The Planck collaboration has obtained a constraint on the nonlinearity parameter in DBI model. To obtain this constraint, the Planck team has used the following bispectrum of the primordial perturbations [35, 36]

$$\mathcal{B}_\Phi(k_1, k_2, k_3) = \frac{6\mathcal{A}^2 f_{NL}}{(k_1 k_2 k_3)^3} \frac{-3}{7(k_1 + k_2 + k_3)^2} \left[\sum_i k_i^5 + \sum_{i \neq j} (2k_i^4 k_j - 3k_i^3 k_j^2) + \sum_{i \neq j \neq l} (k_i^3 k_j k_l - 4k_i^2 k_j^2 k_l) \right], \quad (32)$$

where the power spectrum of the potential Φ , $\mathcal{P}_\Phi(k) = \frac{\mathcal{A}}{k^{4-n_s}}$, has been normalized to \mathcal{A}^2 . By constraining the non-separable shape given by the above equation, the Planck collaboration has obtained the value of the nonlinearity parameter as $f_{NL} = 15.6 \pm 37.3$ from temperature and polarization data at 68% CL [74]. The nonlinearity parameter of the DBI model, given in the above bispectrum, is related to the sound speed of the perturbations.

In the slow-roll approximation, the important terms in the amplitude of the non-Gaussianity are as follows [34]

$$f_{NL} = f_{NL}^\sigma + f_{NL}^c \quad (33)$$

with

$$f_{NL}^\sigma = -\frac{5}{81} \left(\frac{1}{c_s^2} - 1 - \frac{2\sigma}{\Sigma} \right) + (3 - 2c_1) \frac{l\sigma}{\Sigma}, \quad (34)$$

and

$$f_{NL}^c = \frac{35}{108} \left(\frac{1}{c_s^2} - 1 \right), \quad (35)$$

where $c_1 \approx 0.577$ is the Euler constant and

$$\sigma = X^2 P_{,XX} + \frac{2}{3} X^3 P_{,XXX}, \quad (36)$$

$$\Sigma = XP_{,X} + 2X^2P_{,XX}, \quad (37)$$

$$l = \frac{\dot{\sigma}}{\sigma H}. \quad (38)$$

In the above equations, X means derivative with respect to X and a dot shows the derivative with respect to the time. If we consider the DBI model in which

$$P(X, \phi) = -f^{-1}(\phi)\sqrt{1 - 2Xf(\phi)} - V(\phi), \quad (39)$$

the leading order contribution in f_{NL}^σ vanishes [34]. In this regard, only equation (35) contributes in the amplitude of the non-Gaussianity.

Therefore, we have [34, 35, 36]

$$f_{NL} = -\frac{35}{108} \left(\frac{1}{c_s^2} - 1 \right). \quad (40)$$

So, by having the values of the nonlinearity parameter, it is possible to get some constraints on the sound speed. Indeed, the Planck team by using the constraint on f_{NL} at 95% CL and equation (40) has obtained constraints on the sound speed at 95% CL. The constraints are as $c_s \geq 0.069$ from temperature data only at 95% CL, and $c_s \geq 0.087$ from temperature and polarization data at 95% CL.

2.2 Power-Law Inflation in DBI Model

Now, we study the power law inflation which is described by the following scale factor

$$a = a_0 t^n, \quad (41)$$

leading to the following Hubble parameter

$$H(N) = n e^{-\frac{N}{n}}. \quad (42)$$

Actually, the scale factor (41) leads to $H = \frac{n}{t}$, which in terms of the e-fold's number is written as (42). By adopting the power law inflation, the slow-roll parameters take the following form

$$\epsilon_{\pm} = \frac{\left(3n^{\frac{3}{2}}\sqrt{3n-8} \pm 3\sqrt{3}n^2 + 4\sqrt{n}\sqrt{3n-8} \mp 8\sqrt{3}n \right)^2}{n^2 \left(\sqrt{n}\sqrt{3n-8}\sqrt{3} \pm 3n \pm 4 \right)^2 (3n-8)}, \quad (43)$$

$$\eta_{\pm} = 4 \frac{\mp 9\sqrt{3}n^3 \pm 12n^2\sqrt{3} + 9n^{\frac{5}{2}}\sqrt{3n-8} \pm 32\sqrt{3}n + 8\sqrt{n}\sqrt{3n-8}}{n^{\frac{3}{2}} \left(\sqrt{n}\sqrt{3n-8}\sqrt{3} \mp 3n \mp 4 \right)^2 \sqrt{3n-8}}, \quad (44)$$

$$s = 0. \quad (45)$$

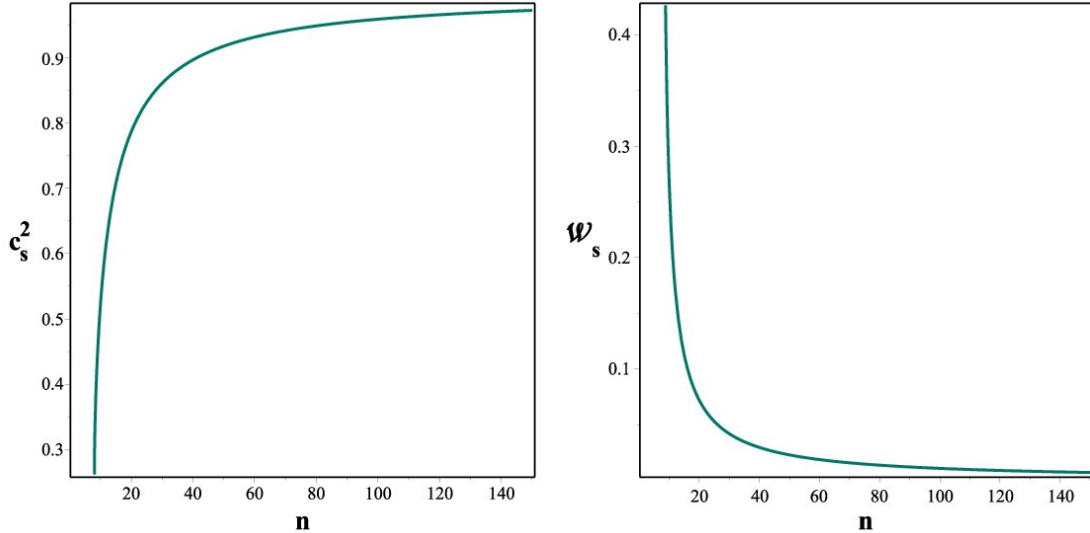


Figure 1: c_s^2 and \mathcal{W}_s versus n in the DBI model with power-law scale factor as $a = a_0 t^n$ and V_+ . As figures show, for all values of n , the DBI model is free of the gradient and ghost instabilities and also satisfies the causality requirement.

By using the above relations, the scalar spectral index, its running and tensor-to-scalar ratio can be expressed in terms of N and n and explored numerically. However, note that the tensor-to-scalar ratio is corresponding to the sound speed (see equations (25) and (26)). On the other hand, as we have stated earlier, to avoid the instabilities, the sound speed of the perturbations should be as $0 < c_s^2 \leq 1$. DBI power-law inflation for some values of n is free of the gradient instabilities and also satisfies the causality requirement for both cases with V_+ and V_- . The left panel of figure 1 shows the evolution of the square of the sound speed versus n for the case with V_+ . For all values of $n \geq 8$, the sound speed is positive and also smaller than unity. The right panel of figure 1 shows evolution of \mathcal{W}_s versus n . As figure shows, for all values of $n \geq 8$ this model is free of ghost instabilities too.

Now, we find the constraints on the parameter n by exploring the observational viability of the tensor-to-scalar ratio, in confrontation with the Planck2018 TT, TE, EE+lowEB+lensing data. By using equations (10), (25) and (44), for V_+ we find

$$r < 0.16 \left(\Lambda\text{CDM} + r + \frac{dn_s}{d \ln k} \right) \implies n \geq 97.914. \quad (46)$$

Now, from the constraint obtained on n we can constraint the sound speed of the model as

$$n \geq 97.914 \implies c_s \geq 0.97914. \quad (47)$$

By implying this constraint on equation (40), we find

$$c_s \geq 0.97914 \implies -0.01395 \leq f_{NL} \leq 0. \quad (48)$$

Therefore, in the power law DBI inflation the amplitude of the non-gaussianity is small. However, the obtained range of n doesn't lead to the observationally viable values of the scalar spectral index.

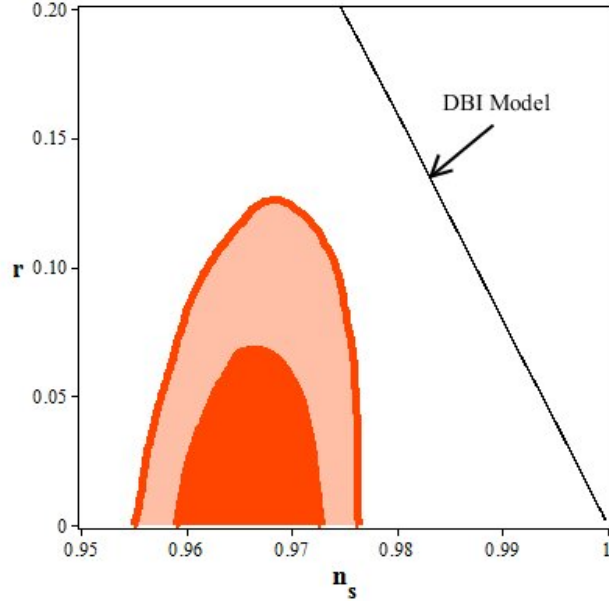


Figure 2: Tensor-to-scalar ratio versus the scalar spectral index for DBI inflation with power law scale factor as $a = a_0 t^n$ and V_+ in the background of Planck2018 TT, TE, EE+lowE+lensing data. This model is not observationally viable.

Actually, considering the scalar spectral index in the $\Lambda\text{CDM}+r+\frac{dn_s}{d\ln k}$ model, as $n_s = 0.9647 \pm 0.0044$ from Planck2018 TT, TE, EE+lowEB+lensing data, gives the following constraint on n

$$50.378 \leq n \leq 64.725. \quad (49)$$

In fact, if we plot r - n_s diagram in the background of Planck2018 TT, TE, EE+lowE+lensing data, it is completely out of the 68% and 95% confidence levels of the data set (see figure 2). In this regard, the power law inflation in DBI model is not observationally viable. Also, in this case there is no running of the scalar spectral index.

We can also study the case corresponding to V_- . With this potential, the behavior of the square of the sound speed is as the left panel of figure 3. As figure shows, in this case also, the DBI power law model with V_- , for $n \geq 8$ is free of the gradient instabilities and also satisfies the causality requirement. The right panel of figure 3 shows the ghost instability issue. As figure shows, the DBI power law model with V_- suffers from ghost instability. By using equations (10), (25) and (44), for V_+ we find the following constraint on n

$$r < 0.16 \left(\Lambda\text{CDM} + r + \frac{dn_s}{d\ln k} \right) \implies n \geq 15.373. \quad (50)$$

On the other hand, numerically exploring the tensor-to-scalar ratio gives another constraint on n . By using equations (19) and (43)-(45), and considering $n_s = 0.9647 \pm 0.0044$ from Planck2018 TT,TE,EE+lowEB+lensing data, we get

$$50.378 \leq n \leq 64.725. \quad (51)$$

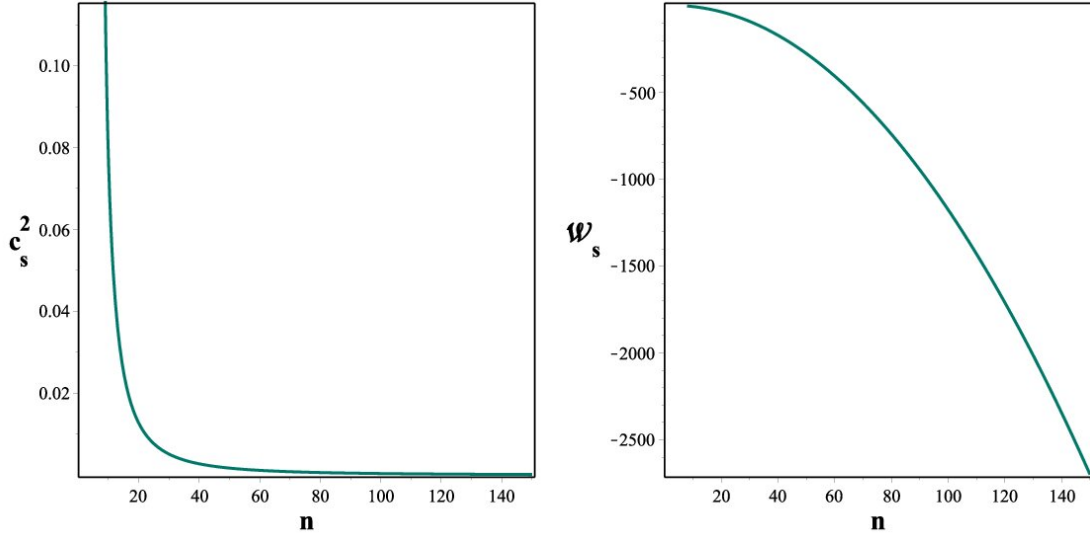


Figure 3: c_s^2 and \mathcal{W}_s versus n in the DBI model with power-law scale factor $a = a_0 t^n$ and V_- . As the left panel shows, for all values of n , the DBI model is free of the gradient instabilities and also satisfies the causality requirement. However, this model suffers from the ghost instabilities as the right panel shows.

This constraint limits the one obtained by exploring the tensor-to-scalar ratio. Now, to obtain the constraint on the sound speed of the perturbations in this model, we study $r - n_s$ plane and find

$$45.1 \leq n \leq 85.1 \implies 0.04408 \leq c_s \leq 0.04651. \quad (52)$$

We note that, instead of using the constraint on n and definition of the sound speed, one can use relation (25) and observationally viable values of r to obtain the observational constraint on the sound speed [86]. This constraint on the sound speed leads to the following constraint on the amplitude of the non-Gaussianity

$$0.04408 \leq c_s \leq 0.04651 \implies -9.63 \times 10^5 \leq f_{NL} \leq -6.93 \times 10^4, \quad (53)$$

which is too large to be consistent with observational data.

We conclude this section that the DBI model with action (3) and a power-law scale factor is not consistent with Planck2018 observational data. A question then arises: how can this tension be overcome? In the next section, we are going to study the DBI model in the *mimetic gravity* framework hoping to overcome this issue. As we shall see, the Mimetic DBI (MDBI) model with power-law scale factor in some subspaces of the model parameter space is consistent with Planck2018 TT, TE, EE+lowE+lensing data.

2.3 Mimetic DBI Model

We construct a DBI cosmological model in the spirit of mimetic gravity. The action of this DBI mimetic gravity, by considering the Lagrange multiplier and a potential term, is constructed as

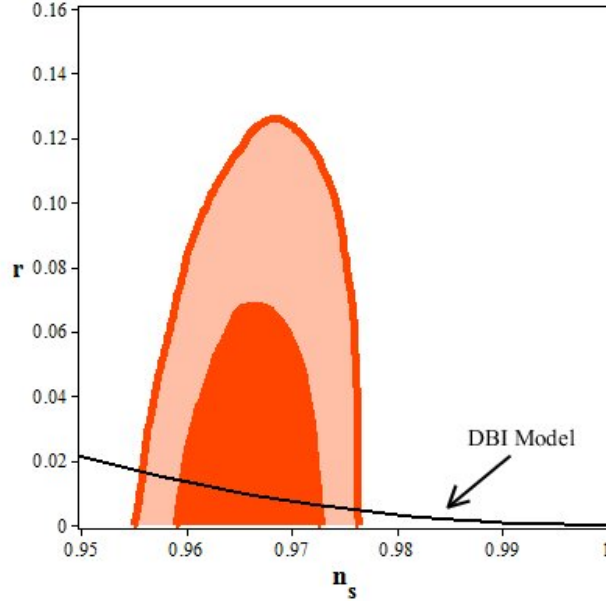


Figure 4: Tensor-to-scalar ratio versus the scalar spectral index in the DBI model with power-law scale factor as $a = a_0 t^n$ and V_- in the background of Planck2018 TT, TE, EE+lowE +lensing data.

follows

$$S = \int d^4x \sqrt{-g} \left[\frac{1}{2\kappa^2} R - f^{-1}(\phi) \sqrt{1 - 2f(\phi)X} + \lambda(g^{\mu\nu} \partial_\mu \phi \partial_\nu \phi + 1) - V(\phi) \right], \quad (54)$$

where, λ is a Lagrange multiplier which lets us to enter the mimetic constraint (2) in the action. We note that one may argue that this action cannot provide a propagating curvature perturbation since if one exerts the mimetic constraint $g^{\mu\nu} \partial_\mu \phi \partial_\nu \phi = -1$ in the DBI term, this term effectively behaves like a potential term ($\sqrt{1 - f(\phi)}$) and therefore the action (54) is equivalent to the original mimetic scenario. However, this is not actually the case since in Lagrangian formalism one is not allowed to impose the constraints on the action from the beginning. The constraints should be imposed on equations of motion just after derivation of the equations. With this point in mind, as we will show action (54) provides propagating curvature perturbation ($c_s \neq 0$). We note also that in the original mimetic scenario, to have propagating curvature perturbation (with nonzero sound speed) the authors added the higher derivative term $(\square\phi)^2$ (see Ref. [5] for details). Here we are able to provide such a propagating modes in a mimetic DBI scenario without additional $(\square\phi)^2$ term, provided that the mimetic constraint to be imposed after derivation of the field equations.

Varying the action (54) with respect to λ recovers the constraint equation (2). Variation of the

action with respect to the metric leads to the following Einstein's field equations

$$G_{\mu\nu} = \kappa^2 \left[-g_{\mu\nu} f^{-1} \sqrt{1 + f g^{\mu\nu} \partial_\mu \phi \partial_\nu \phi} - g_{\mu\nu} V + g_{\mu\nu} \lambda \left(g^{\mu\nu} \partial_\mu \phi \partial_\nu \phi + 1 \right) + \partial_\mu \phi \partial_\nu \phi \left(1 + f g^{\mu\nu} \partial_\mu \phi \partial_\nu \phi \right)^{-\frac{1}{2}} - 2\lambda \partial_\mu \phi \partial_\nu \phi \right]. \quad (55)$$

With the flat FRW metric (5) the Einstein's field equations (55) lead to the following Friedmann equations

$$3H^2 = \kappa^2 \left[\frac{f^{-1}}{\sqrt{1 - f\dot{\phi}^2}} + V - \lambda(1 + \dot{\phi}^2) \right], \quad (56)$$

$$2\dot{H} + 3H^2 = \kappa^2 \left[f^{-1} \sqrt{1 - f\dot{\phi}^2} + V + \lambda(\dot{\phi}^2 - 1) \right]. \quad (57)$$

Variation of the action (54) with respect to ϕ gives the following equation of motion

$$\frac{\ddot{\phi}}{(1 - f\dot{\phi}^2)^{\frac{3}{2}}} + \frac{3H\dot{\phi}}{(1 - f\dot{\phi}^2)^{\frac{1}{2}}} - 2\lambda(\ddot{\phi} + 3H\dot{\phi}) + V' - \lambda'(1 - \dot{\phi}^2) = -\frac{f'}{f^2} \left[\frac{3f\dot{\phi}^2 - 2}{2(1 - f\dot{\phi}^2)^{\frac{1}{2}}} \right]. \quad (58)$$

The slow-roll parameters in the MDBI model are given by equations (9), however, the Hubble parameter and sound speed take new forms. The Hubble parameter is given by the Friedmann equation (56) and the square of sound speed is defined as

$$c_s^2 = \frac{\left(1 - f\dot{\phi}^2\right)^{-\frac{1}{2}} - 2\lambda}{\left(1 - f\dot{\phi}^2\right)^{-\frac{3}{2}} - 2\lambda}. \quad (59)$$

In the MDBI model, the tensor-to-scalar ratio and the scalar spectral index are defined by equations (15) and (16), where the amplitudes of the perturbations are given by (17) and (23).

In fact, now the amplitude of the scalar perturbation is given by

$$\mathcal{A}_s = \frac{H^2}{8\pi^2 \mathcal{W}_s c_s^3} = \frac{H^2}{8\pi^2 (\mathcal{W}_s^{(DBI)} + \lambda W) c_s^3}, \quad (60)$$

where we have used $\mathcal{W}_s = \mathcal{W}_s^{(DBI)} + \lambda W$, with

$$W = \frac{\left(f \dot{\phi}^2 \sqrt{1 - f\dot{\phi}^2} - \sqrt{1 - f\dot{\phi}^2} \right) \dot{\phi}^2}{2H^2 \left(1 - f\dot{\phi}^2 \right)^{3/2}}. \quad (61)$$

and $\mathcal{W}_s^{(DBI)}$ is given by the equation (18).

This means that in the MDBI model, the parameter \mathcal{W}_s is given by

$$\mathcal{W}_s = \frac{\left(f \dot{\phi}^2 \lambda \sqrt{1 - f \dot{\phi}^2} - \lambda \sqrt{1 - f \dot{\phi}^2 + 1} \right) \dot{\phi}^2}{2H^2 \left(1 - f \dot{\phi}^2 \right)^{3/2}}. \quad (62)$$

In the case with $\lambda = 0$, the above equations reduce to the ones obtained in ordinary DBI setup. Although we have derived a new \mathcal{W}_s , but we can still use equations (19), (20) and (25) for the scalar spectral index, its running and tensor-to-scalar ratio (where, the slow-roll parameters and sound speed are now corresponding to the MDBI model).

For instance, the tensor-to-scalar ratio in the MDBI model becomes

$$r = 16 \left(\frac{\left(1 - f \dot{\phi}^2 \right)^{-\frac{1}{2}} - 2\lambda}{\left(1 - f \dot{\phi}^2 \right)^{-\frac{3}{2}} - 2\lambda} \right)^{\frac{1}{2}} \epsilon, \quad (63)$$

or

$$r = -8 \left(\frac{\left(1 - f \dot{\phi}^2 \right)^{-\frac{1}{2}} - 2\lambda}{\left(1 - f \dot{\phi}^2 \right)^{-\frac{3}{2}} - 2\lambda} \right)^{\frac{1}{2}} n_T. \quad (64)$$

Here also, if we take $\lambda = 0$ the above equations become the same as equations (25) and (26).

Also, to seek for the non-Gaussian features of the primordial perturbations we can use equation (31), (32) and (40). It is important to notice that, although our model is the MDBI model, but the relations (31), (32) and (40) are applicable. This is because the MDBI model is still $P(X, \phi)$ one and the differences appear in the definitions of the slow-roll parameters and also the sound speed.

This is because for the MDBI model $P(X, \phi)$ is given by

$$P(X, \phi) = -f^{-1}(\phi) \sqrt{1 - 2X f(\phi)} - V(\phi) + \lambda(1 - 2X) \quad (65)$$

which differs from $P(X, \phi)$ of the DBI model in $\lambda(1 - 2X)$ term. This term is linear in X , so there would be no change in the contribution of equation (34) and we end up with the amplitude of the non-Gaussianity as given by equation (40).

The Lagrange Multiplier λ in equations (55)-(62) is not determined yet. This parameter can be found by taking trace of the Einstein's field equation (55). However, we don't track this way. As before, following Refs. [61, 62], we use the Friedmann equations to obtain the Lagrange Multiplier and potential in terms of the Hubble parameter and its derivatives. Here also, we adopt $f^{-1}(\phi) =$

$V(\phi)$. Now, by considering $\phi = t$, leading to $\dot{\phi} = 1$, equation (57) gives the following expression for the potential

$$V = \frac{\left[2H(N)H'(N) + 3H^2(N)\right]^2}{\kappa^2 \left[-\kappa^2 + 4H(N)H'(N) + 6H^2(N)\right]}, \quad (66)$$

where a prime shows a derivative of the parameter with respect to N . We can obtain the Lagrange Multiplier from equations (56) and (66) as follows

$$\lambda = \frac{9H^4B - 3H^2B\kappa^2 - 9H^4 - 12H^3H' - 4H^2H'^2B - 4H^2H'^2}{-2AB\kappa^2}, \quad (67)$$

where $H = H(N)$ and

$$A = 6H^2 + 4HH' - \kappa^2, \quad B = \sqrt{1 - \frac{\kappa^2 A}{(3H^2 + 2HH')^2}}. \quad (68)$$

We also find the following expressions for the slow-roll parameters in terms of the Hubble parameter and its derivatives

$$\epsilon = \frac{\kappa}{2} \sqrt{-\frac{2H'}{H^3}}, \quad (69)$$

$$\eta = \frac{\sqrt{2}\kappa}{4} \frac{(HH'' + H'^2)}{(-HH')^{\frac{3}{2}}}. \quad (70)$$

The third parameter s is lengthy and has been shifted to the Appendix. By having the slow-roll parameters, we can write the scalar spectral index, its running and the tensor-to-scalar ratio in terms of the Hubble parameter and its derivatives to explore them numerically.

2.4 Power-Law Inflation in Mimetic DBI Model

To study the power-law inflation in MDBI model, we use the scale factor defined in equation (41), corresponding to the Hubble parameter (42). By this scale factor, the slow-roll parameters in the MDBI model take the following form

$$\epsilon = \eta = \frac{1}{2} \frac{\sqrt{2}\kappa e^{\frac{N}{n}}}{n^{\frac{3}{2}}}, \quad (71)$$

$$\begin{aligned} s = & -\frac{\sqrt{2}}{2} e^{-\frac{N}{n}} \left(108e^{-2\frac{N}{n}} n^4 - 216e^{-2\frac{N}{n}} n^3 + 144n^2 e^{-2\frac{N}{n}} - 9n^2 \kappa^2 - 32ne^{-2\frac{N}{n}} + 12n\kappa^2 - 4\kappa^2\right) \\ & \kappa^5 n^{-\frac{3}{2}} \left(3n^2 e^{-2\frac{N}{n}} - 2ne^{-2\frac{N}{n}} - \kappa^2\right)^{-1} \left(54e^{-6\frac{N}{n}} n^5 - 108e^{-6\frac{N}{n}} n^4 + 72e^{-6\frac{N}{n}} n^3 - 54n^3 e^{-4\frac{N}{n}} \kappa^2 \right. \\ & \left. - 16e^{-6\frac{N}{n}} n^2 + 72n^2 e^{-4\frac{N}{n}} \kappa^2 + 18n^2 e^{-2\frac{N}{n}} \kappa^4 - 24ne^{-4\frac{N}{n}} \kappa^2 - 6ne^{-2\frac{N}{n}} \kappa^4 - 4e^{-2\frac{N}{n}} \kappa^4 - 3\kappa^6\right)^{-1}. \end{aligned} \quad (72)$$

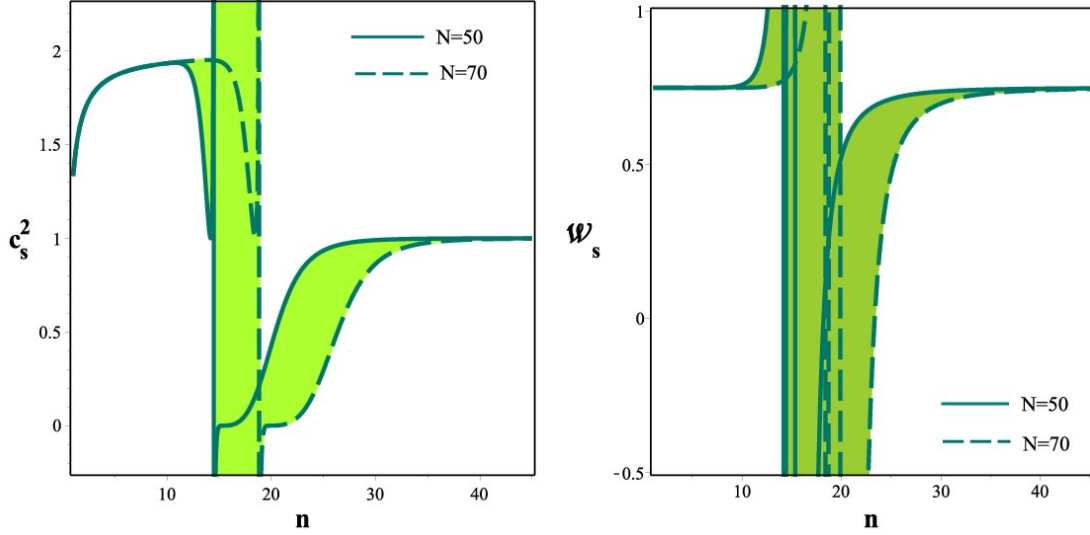


Figure 5: c_s^2 and \mathcal{W}_s versus n in the MDBI inflation with power-law scale factor as $a = a_0 t^n$. The colored regions are free of instabilities. Note that there is overlap between these regions in two panels.

By using the above relations, the scalar spectral index, its running and tensor-to-scalar ratio can be expressed in terms of N and n and then explored numerically. However, we first analyze the stability issue in the MDBI model. We study c_s^2 and \mathcal{W}_s numerically to find some subspaces of the model parameters space for which the model is free of gradient and ghost instabilities. In the left panel of figure 5, we see the behavior of the sound speed versus n in the interval $50 \leq N \leq 70$. Our numerical analysis shows that for $N = 50$ the MDBI model is free of gradient instabilities and also satisfies the causality requirement if $n \leq 14.6$. For $N = 60$, it is free of the gradient instabilities and satisfies the causality requirement if $n \leq 16.7$. Also, for $N = 70$, the constraint on n in order to get rid of gradient instabilities is $n \leq 19$. Table 1 shows the viable ranges of n for several sample values of N . In the right panel of figure 5, we see the behavior of \mathcal{W}_s versus n in the interval $50 \leq N \leq 70$. Our numerical analysis shows that for $N = 50$, in the domains $n \leq 15.3$ and $n \geq 18.2$, the parameter \mathcal{W}_s is positive and therefore the power-law MDBI model is free of the ghost instability. For $N = 60$, in the domains $n \leq 17.6$ and $n \geq 20.9$, and also for $N = 70$, in the domains $n \leq 19.8$ and $n \geq 23.4$, the parameter \mathcal{W}_s is positive and the model is free of ghost instability. Table 2 shows the acceptable ranges of n , leading to positive \mathcal{W}_s for several sample values of N . So, regarding the stability issue of the MDBI model, there are some subspaces of the model parameters space that the model is free of the ghost and gradient instabilities.

Now, we find some constraints on the parameter n by exploring the observational viability of n_s , r and α_s , in confrontation with the Planck2018 dataset. Firstly, we study n_s , r and α_s separately. The results are shown in figure 6. The upper-left panel of figure 6 shows the parameters space of the MDBI model which leads to $n_s = 0.9647 \pm 0.0044$. Our numerical analysis shows that for $N = 50$ the scalar spectral index would be viable if $39.71 \leq n \leq 43.55$. For $N = 60$ we get the viable scalar spectral index if $43.25 \leq n \leq 47.29$. For $n = 70$ the scalar spectral index is viable if $46.665 \leq n \leq 50.75$. The upper-right panel of figure 6 shows the parameter space of the MDBI model leading to the observationally viable values of the tensor-to-scalar ratio. Based on this

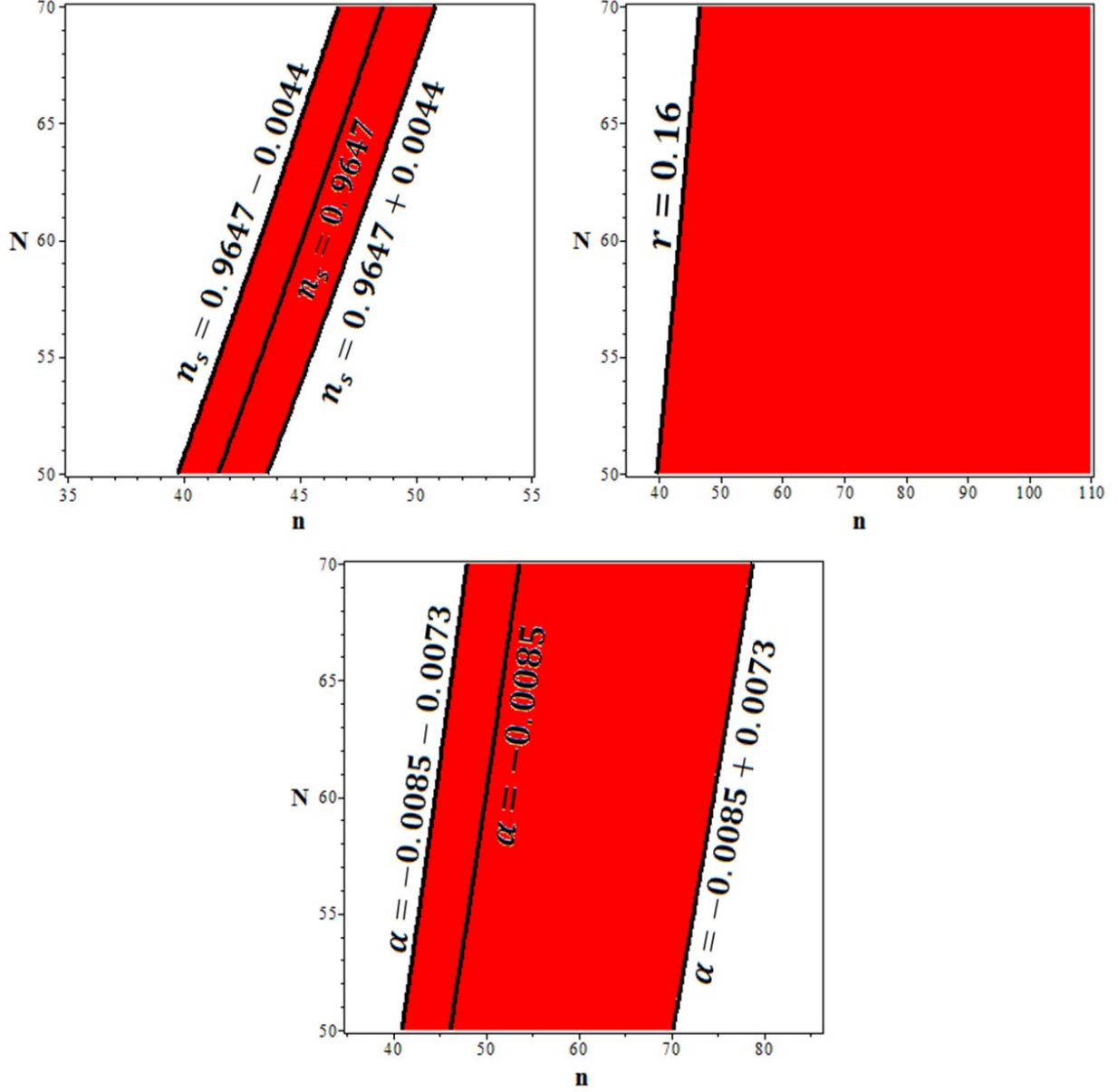


Figure 6: The ranges of parameters n and N which lead to the observationally viable values of the scalar spectral index (upper-left panel), the tensor-to-scalar ratio (upper-right panel) and the running of the scalar spectral index (lower panel) in the MDBI model with $a = a_0 t^n$. The adopted values of n_s , r and α_s are from Planck2018 TT, TE, EE+low EB+lensing data, in Λ CDM+ $r + \frac{dn_s}{d \ln k}$ model.

Table 1: The ranges of n in which the MDBI model is free of the gradient instabilities and also satisfies the causality requirement. The ranges are obtained for some sample values of the number of e-folds.

| N | 50 | 55 | 60 | 65 | 70 |
|------|---------------|---------------|---------------|---------------|-------------|
| MDBI | $14.6 \leq n$ | $15.6 \leq n$ | $16.7 \leq n$ | $17.8 \leq n$ | $19 \leq n$ |

Table 2: The ranges of n in which the MDBI model is free of the ghost instabilities. The ranges are obtained for some sample values of the number of e-folds.

| N | 50 | 55 | 60 | 65 | 70 |
|------|-------------------------------------|-------------------------------------|-------------------------------------|-------------------------------------|-------------------------------------|
| MDBI | $n \leq 15.3$ & $18.2 \leq n$ | $n \leq 16.5$ & $19.6 \leq n$ | $n \leq 17.6$ & $20.9 \leq n$ | $n \leq 18.7$ & $22.1 \leq n$ | $n \leq 19.8$ & $23.4 \leq n$ |

numerical analysis, the tensor-to-scalar is observationally viable if $n \geq 39.21$ for $N = 50$, $n \geq 43.02$ for $N = 60$ and $n \geq 46.07$ for $N = 70$. The lower panel of figure 6 shows the parameter space of the MDBI model leading to the observationally viable values of the running of the scalar spectral index. This numerical analysis shows that the running of the scalar spectral index is observationally viable if $40.79 \leq n \leq 70.23$ for $N = 50$, $44.51 \leq n \leq 74.55$ for $N = 60$ and $47.78 \leq n \leq 78.81$ for $N = 70$.

Although by studying n_s , r and α_s we have obtained some constraints on the parameter n , however, it is useful to find the constraints by exploring $\alpha_s - n_s$ and $r - n_s$ behavior in comparison to the Planck2018 data. We have performed numerical analysis to obtain some constraints on the parameter n . These constraints show the ranges of the parameters in which both the scalar spectral index and tensor-to-scalar ratio are consistent with Planck2018 data. Scalar spectral index versus the running of the scalar spectral index is shown in figure 7, where we have used the Planck2018 TT, TE, EE+lowE+lensing data at 68% and 95% CL in the background. In this figure, we have plotted n_s versus α_s for three values of the e-folds number as $N = 50, 60$ and 70 . As figure shows, $\alpha_s - n_s$ plane in the MDBI model lies in the 68% and 95% CL of the Planck2018 TT, TE, EE+low E+lensing data. By using this dataset, we have obtained some constraints on n . Our numerical analysis shows that, $\alpha_s - n_s$ in the MDBI model is observationally viable if $38.7 \leq n \leq 47.6$ for $N = 50$, $42.2 \leq n \leq 51.2$ for $N = 60$ and $45.6 \leq n \leq 54.9$ for $N = 70$. In table 3 the constraints obtained for some sample values of the e-folds number are presented. Figure 8 shows the tensor-to-scalar ratio versus the scalar spectral index in the MDBI model, in the background of the Planck2018 TT, TE, EE+low E+lensing data at the 68% and 95% CL, for $N = 50, 60$ and 70 . Although $r - n_s$ planes for all three values of the e-folds number overlap, however, the observationally viable ranges of n are different for each cases. Our numerical analysis shows that $r - n_s$ in the MDBI model is observationally viable if $43.3 \leq n \leq 46.2$ for $N = 50$, $47.0 \leq n \leq 50.1$ for $N = 60$ and $50.5 \leq n \leq 53.5$ for $N = 70$. In table 4 the constraints obtained for some sample values of the e-folds number are presented. Note that, the constraints obtained

Table 3: The ranges of n in which both the scalar spectral index and its running in the MDBI inflation are consistent with 95% CL of the Planck2018 TT, TE, EE+low E+lensing data.

| N | 50 | 55 | 60 | 65 | 70 |
|-----|-------------------------|-------------------------|-------------------------|-------------------------|-------------------------|
| | $37.9 \leq n \leq 47.2$ | $39.7 \leq n \leq 49.1$ | $41.5 \leq n \leq 50.7$ | $43.1 \leq n \leq 52.6$ | $44.8 \leq n \leq 54.3$ |

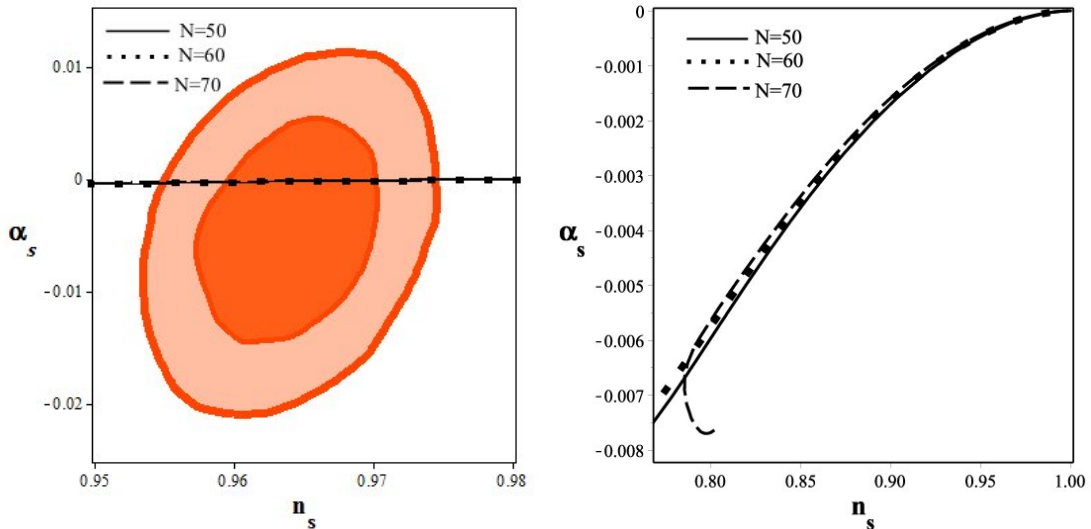


Figure 7: Running of the scalar spectral index versus the scalar spectral index of the MDBI model in the background of the Planck2018 TT, TE, EE+lowE+lensing data. In the right panel we have zoomed out the evolution of α_s versus n_s .

from $r - n_s$ analysis are the subsets of the ones obtained by analyzing $\alpha_s - n_s$. Therefore, these constraints are more viable in the sense of leading to observationally viable behavior of both $r - n_s$ and $\alpha_s - n_s$. In this regard, we use the constraint obtained from $r - n_s$ analysis to constraint the sound speed of the model and non-Gaussian feature. In table 4, you also see the constraints on c_s and f_{NL} corresponding to the observationally viable values of the scalar spectral index, its running and tensor-to-scalar ratio. Figure 9 shows the nonlinearity parameter versus the sound speed in the MDBI model. The right panel of this figure shows the observationally viable ranges of the nonlinearity parameter which is obtained from the viable values of the sound speed in this model. According to our numerical analysis, the MDBI model with power-law scale factor is consistent with observational data for some ranges of n and predicts small amplitudes of the non-Gaussianity.

3 Constant Sound Speed

In this section, we consider the case in which the sound speed is constant and study the DBI and MDBI models with constant c_s . In this section, we use the Planck constraint on f_{NL} and c_s to obtain the observationally viable values of n . In fact, for some constant values of the sound speed-

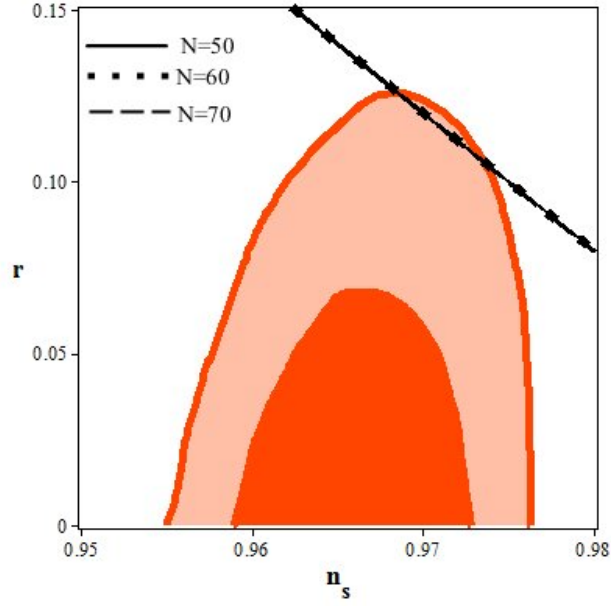


Figure 8: Tensor-to-scalar ratio versus the scalar spectral index in MDBI model with $a = a_0 t^n$ in the background of Planck2018 TT, TE, EE+low E+lensing data.

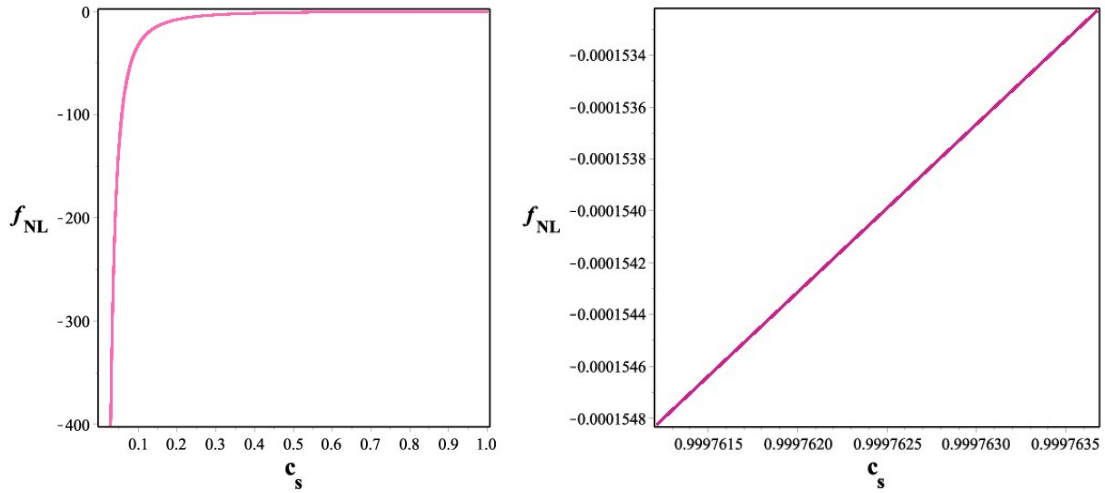


Figure 9: The nonlinearity parameter versus the sound speed in MDBI model with $a = a_0 t^n$ (left panel). The observationally viable ranges of the nonlinearity parameter and sound speed in this model, obtained from the constraints on n (right panel).

Table 4: The ranges of n in which both the scalar spectral index and the tensor-to-scalar ratio in the MDBI inflation are consistent with 95% CL of the Planck2018 TT, TE, EE+low E+lensing data. The table also shows the constraints on the sound speed and the nonlinearity parameter corresponding to the constraints on n .

| | | | |
|----------|-------------------------|--|--|
| $N = 50$ | $43.3 \leq n \leq 46.2$ | $-0.20214 \times 10^{-3} \leq \alpha_s \leq -0.14817 \times 10^{-3}$ | $0.99978 \leq c_s \leq 0.99987$ $-0.13764 \times 10^{-3} \leq f_{NL} \leq -0.846199 \times 10^{-4}$ |
| $N = 55$ | $45.1 \leq n \leq 48.1$ | $-0.19870 \times 10^{-3} \leq \alpha_s \leq -0.14482 \times 10^{-3}$ | $0.99976 \leq c_s \leq 0.99985$ $-0.15777 \times 10^{-3} \leq f_{NL} \leq -0.95739 \times 10^{-4}$ |
| $N = 60$ | $47.0 \leq n \leq 50.1$ | $-0.19273 \times 10^{-3} \leq \alpha_s \leq -0.13989 \times 10^{-3}$ | $0.99973 \leq c_s \leq 0.99984$ $-0.17508 \times 10^{-3} \leq f_{NL} \leq -0.10517 \times 10^{-3}$ |
| $N = 65$ | $48.8 \leq n \leq 52.0$ | $-0.18862 \times 10^{-3} \leq \alpha_s \leq -0.13626 \times 10^{-3}$ | $0.99969 \leq c_s \leq 0.99982$ $-0.19512 \times 10^{-3} \leq f_{NL} \leq -0.11594 \times 10^{-3}$ |
| $N = 70$ | $50.5 \leq n \leq 53.5$ | $-0.15809 \times 10^{-3} \leq \alpha_s \leq -0.11817 \times 10^{-4}$ | $0.99966 \leq c_s \leq 0.99979$ $-0.21862 \times 10^{-3} \leq f_{NL} \leq -0.13446 \times 10^{-3}$ |

which is corresponding to the observationally viable values of nonlinearity parameter- we study $r - n_s$ and $\alpha_s - n_s$ and find some constraints on n . The background equations are the same as the previous sections but now with constant sound speed. However, the potential and Lagrange multiplier change and therefore some parameters such as the slow-roll parameters, scalar spectral index and tensor-to-scalar ratio change accordingly. We start the issue with DBI model.

3.1 DBI model

To obtain the DBI parameter f in terms of the sound speed, we use equation (10). The result is as follows

$$f = \frac{1}{2} \frac{\kappa^2 (c_s^2 - 1)}{HH'}. \quad (73)$$

By substituting this expression for f in equation (6), we find the potential of the model as

$$V = -\frac{H(-3c_s^3 H + 3H c_s + 2H')}{\kappa^2 (c_s^2 - 1) c_s}. \quad (74)$$

Now, by having the functions f and V , we use equations (6), (9) and (41) to find the following slow-roll parameters

$$\epsilon = \frac{9c_s^6 n^2 - 18c_s^4 n^2 + 12nc_s^3 - 12c_s^4 n + 9c_s^2 n^2 - 12nc_s + 12c_s^2 n - 8c_s + 4c_s^2 + 4}{n(3c_s^3 n - 3c_s n + 2 - 2c_s)^2}, \quad (75)$$

$$\eta = -\frac{1}{2} \left(6c_s^6 n e^{-4\frac{N}{n}} \kappa^2 - 9c_s^6 n^3 e^{-6\frac{N}{n}} - 12c_s^4 n e^{-4\frac{N}{n}} \kappa^2 + 18c_s^4 n^3 e^{-6\frac{N}{n}} + 4e^{-4\frac{N}{n}} c_s^3 \kappa^2 + 4e^{-4\frac{N}{n}} c_s^4 \kappa^2 \right. \\ \left. - 12n^2 e^{-6\frac{N}{n}} c_s^3 + 12c_s^4 n^2 e^{-6\frac{N}{n}} + 6c_s^2 n e^{-4\frac{N}{n}} \kappa^2 - 9c_s^2 n^3 e^{-6\frac{N}{n}} - 4e^{-4\frac{N}{n}} c_s \kappa^2 - 4e^{-4\frac{N}{n}} c_s^2 \kappa^2 \right. \\ \left. + 12n^2 e^{-6\frac{N}{n}} c_s - 12c_s^2 n^2 e^{-6\frac{N}{n}} + 8n e^{-6\frac{N}{n}} c_s - 4n e^{-6\frac{N}{n}} c_s^2 - 4n e^{-6\frac{N}{n}} \right) \frac{e^{6\frac{N}{n}} n^{-2}}{\left(3c_s^3 n - 3c_s n + 2 \right)^2}. \quad (76)$$

In this case also, the third slow-roll parameter, s , is zero. After obtaining the slow-roll parameters, we can find scalar spectral index, its running and tensor-to-scalar ratio and then analyze the parameters space of the model numerically. Since the sound speed is constant in this section, we can use Planck constraint on this quantity to analyze the model numerically. We adopt some sample values of the sound speed which are larger than 0.087 (the lower limit from Planck2015 temperature and polarization data at 95% CL [74]). Note that, although η is related to the number of e-folds parameter, but it has not an impressive effect on the numerical analysis of the model. In fact, the difference between the values of n_s and r for different values of N is of the order of 10^{-7} . Therefore, the constraint that we obtain, is very nearly independent of the values of the e-folds number. We perform a numerical analysis on the model's parameters for some sample values of the sound speed as $c_s = 0.1, 0.4, 0.7$ and 0.9 . By using these values of c_s , we study $r - n_s$ plane in comparison with Planck2018 TT, TE, EE+lowE+lensing data. The results are shown in figure 10. As this figure shows, the DBI model with constant sound speed and the power-law scale factor, in some ranges of n is consistent with Planck2018 observational data. The ranges of n leading to the observationally viable values of the scalar spectral index and tensor-to-scalar ratio are shown in tables 5 and 6. Then, we study $\alpha_s - n_s$ plane in comparison with Planck2018 TT, TE, EE+lowE+lensing data, as shown in figure 11. In this regard, we obtain the values of the running of the scalar spectral index corresponding to these ranges of n . The results are shown in tables 5 and 6.

Note that, the power-law DBI model, with f and V as given in equations (73) and (74) is ghost free. This is because that in this case, the parameter \mathcal{W} , given by (18), is always positive for values of $n \geq 8$ and $c_s \geq 0.087$.

3.2 Mimetic DBI (MDBI) model

By using equations (56) and (57), we obtain the lagrange multiplier in terms of the brane tension as follows

$$\lambda = \frac{1}{2} \frac{2H' \sqrt{1-f} + \kappa^2}{\sqrt{1-f\kappa^2}}. \quad (77)$$

Now, by using the above equation and equation (59) we find

$$f = - \left[\frac{1}{6} \frac{\sqrt[3]{\kappa^2 c_s^2 (-c_s^4 \kappa^4 + 54 H'^2 c_s^4 - 108 H'^2 c_s^2 + c_s^2 z + 54 H'^2 - z)}}{H' (c_s^2 - 1)} - \frac{1}{6} \frac{\kappa^2 c_s^2}{H' (c_s^2 - 1)} \right. \\ \left. + \frac{1}{6 H' (c_s^2 - 1)} \frac{c_s^4 \kappa^4}{\sqrt[3]{\kappa^2 c_s^2 (-c_s^4 \kappa^4 + 54 H'^2 c_s^4 - 108 H'^2 c_s^2 + c_s^2 z + 54 H'^2 - z)}} \right]^2 + 1, \quad (78)$$

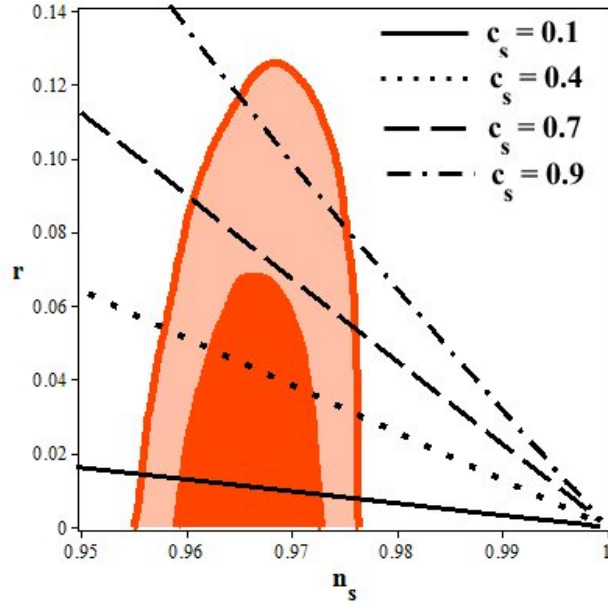


Figure 10: Tensor-to-scalar ratio versus the scalar spectral index for the power-law DBI inflation with constant sound speed in the background of Planck2018 TT, TE, EE+lowE+lensing data.

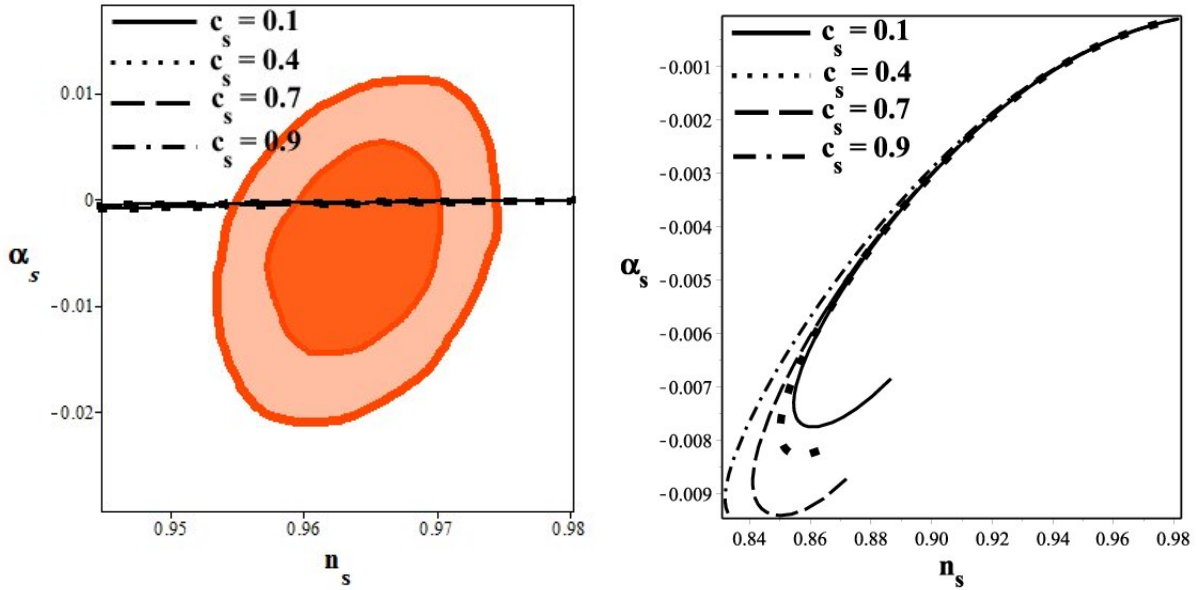


Figure 11: Running of the scalar spectral index versus the scalar spectral index for the power-law DBI inflation with constant sound speed in the background of the Planck2018 TT, TE, EE+lowE+lensing data. In the right panel we have zoomed out the evolution of α_s versus n_s .

Table 5: The ranges of n in which both the scalar spectral index and tensor-to-scalar ratio in the power-law DBI inflation with constant sound speed are consistent with 95% CL of the Planck2018 TT, TE, EE+lowE+lensing data. This table also shows the constraints on the running of the scalar spectral index obtained from the constraints on n .

| c_s | f_{NL} | n | α_s |
|-------|-----------|---------------------------|--|
| 0.1 | -32.08333 | $112.7 \leq n \leq 211.1$ | $-0.58770 \times 10^{-3} \leq \alpha_s \leq -0.16783 \times 10^{-3}$ |
| 0.4 | -1.70139 | $118.5 \leq n \leq 210.3$ | $-0.53110 \times 10^{-3} \leq \alpha_s \leq -0.16899 \times 10^{-3}$ |
| 0.7 | -0.33730 | $126.3 \leq n \leq 208.7$ | $-0.46504 \times 10^{-3} \leq \alpha_s \leq -0.17102 \times 10^{-3}$ |
| 0.9 | -0.07602 | $134.1 \leq n \leq 204.8$ | $-0.40302 \times 10^{-3} \leq \alpha_s \leq -0.17490 \times 10^{-3}$ |

Table 6: The ranges of n in which both the scalar spectral index and tensor-to-scalar ratio in the power-law DBI inflation with constant sound speed are consistent with 68% CL of the Planck2018 TT, TE, EE+lowE+lensing data. This table also shows the constraints on the running of the scalar spectral index obtained from the constraints on n .

| c_s | f_{NL} | n | α_s |
|-------|----------------|---------------------------|--|
| 0.1 | -32.08333 | $123.4 \leq n \leq 181.8$ | $-0.49035 \times 10^{-3} \leq \alpha_s \leq -0.22620 \times 10^{-3}$ |
| 0.4 | -1.70139 | $132.4 \leq n \leq 176.5$ | $-0.42564 \times 10^{-3} \leq \alpha_s \leq -0.23978 \times 10^{-3}$ |
| 0.7 | not consistent | not consistent | not consistent |
| 0.9 | not consistent | not consistent | not consistent |

where

$$z = 6 H' \sqrt{-c_s^4 \kappa^4 + 27 H'^2 c_s^4 - 54 H'^2 c_s^2 + 27 H'^2 \sqrt{3}}. \quad (79)$$

By using equation (57), we obtain the potential as follows

$$V = -\frac{\kappa^2 \sqrt{1-f} - (2 H H' + 3 H^2) f}{f \kappa^2}, \quad (80)$$

where f is given by equation (78). Here, by adopting the scale factor (41), we firstly study possible existence of ghost instability in this model. By substituting equations (77), (78) and (80) in equation (62), we explore \mathcal{W}_s numerically. The results are shown in figure 12, where we have used $50 \leq N \leq 70$ and $c_s = 0.1, 0.4, 0.7, 0.9$. Our numerical analysis shows that, for all values of $n \geq 5$ the parameter \mathcal{W}_s is positive and therefore the power-law MDBI model with constant sound speed is free of ghost instability (in fact, for $n < 5$, the parameter \mathcal{W}_s becomes imaginary).

In this case, the slow-roll parameters take the following form

$$\epsilon = \frac{1}{2} \frac{\sqrt{6} \kappa \left(3 e^{-\frac{N}{n}} n^2 - 2 e^{-\frac{N}{n}} n + 1 \right) e^{\frac{N}{2n}}}{\sqrt{n} \left(3 e^{-\frac{N}{n}} n^2 - 2 e^{-\frac{N}{n}} n + 2 \right)^{-\frac{3}{2}}}, \quad (81)$$

$$\begin{aligned} \eta = -6 \left\{ \frac{\sqrt{3}}{6} \kappa^2 \left[\frac{n}{2} \left(-\frac{8}{n} \left(e^{-\frac{N}{n}} \right)^2 + 12 \left(e^{-\frac{N}{n}} \right)^2 \right) - \frac{1}{2} \frac{\kappa^2 n f''}{f^2 \sqrt{1-f}} + \frac{\kappa^2 n f'^2}{f^3 \sqrt{1-f}} - \frac{1}{2} \frac{\kappa^2 n f'^2}{f^2 (1-f)^{\frac{3}{2}}} \right. \right. \\ \left. \left. + \frac{1}{4} \frac{\kappa^2 n f''}{f (1-f)^{\frac{3}{2}}} + \frac{3}{8} \frac{\kappa^2 n f'^2}{f (1-f)^{\frac{5}{2}}} - \kappa^2 n \lambda' \right] \left[\left(- \left(\kappa^2 \sqrt{1-f} - \left(-2n \left(e^{-\frac{N}{n}} \right)^2 + \frac{1}{f \sqrt{1-f}} - 2\lambda \right. \right. \right. \right. \right. \\ \left. \left. \left. + 3n^2 \left(e^{-\frac{N}{n}} \right)^2 \right) f \right) f^{-1} \right]^{-\frac{1}{2}} - \frac{\sqrt{3}}{12} \kappa^4 \left[\frac{\sqrt{2}}{2} \sqrt{\frac{n}{\kappa^2}} \left(4 \left(e^{-\frac{N}{n}} \right)^2 - 6n \left(e^{-\frac{N}{n}} \right)^2 \right) - \frac{1}{2} \frac{\sqrt{2} \sqrt{\kappa^2 n} f'}{f^2 \sqrt{1-f}} \right. \right. \\ \left. \left. + \frac{1}{4} \frac{\sqrt{2} \sqrt{\kappa^2 n} f'}{f (1-f)^{3/2}} - \sqrt{2} \sqrt{\kappa^2 n} \lambda' \right]^2 \left[\kappa^2 \left(- \left(\kappa^2 \sqrt{1-f} + \left(2n \left(e^{-\frac{N}{n}} \right)^2 - 3n^2 \left(e^{-\frac{N}{n}} \right)^2 \right) f \right) \frac{f^{-1}}{\kappa^2} \right. \right. \right. \\ \left. \left. \left. + \frac{1}{f \sqrt{1-f}} - 2\lambda \right) \right]^{-\frac{3}{2}} \right\} \kappa^{-2} \left(\frac{\sqrt{2}}{2} \sqrt{\kappa^2 n} \left(4 \left(e^{-\frac{N}{n}} \right)^2 - 6n \left(e^{-\frac{N}{n}} \right)^2 \right) \kappa^{-2} \right. \\ \left. - \frac{1}{2} \frac{\sqrt{2} \sqrt{\kappa^2 n} f'}{f^2 \sqrt{1-f}} + \frac{1}{4} \frac{\sqrt{2} \sqrt{\kappa^2 n} f'}{f (1-f)^{3/2}} - \sqrt{2} \sqrt{\kappa^2 n} \lambda' \right)^{-1}, \quad (82) \end{aligned}$$

$$s = \frac{\sqrt{6}}{8} \frac{1}{\sqrt{n}} \frac{\kappa^3 \left(-f f' n + 2 f^2 - 2 f n - 2 f \right) e^{\frac{N}{2n}}}{(f-1) \sqrt{3 e^{-\frac{N}{n}} n^2 - 2 n e^{-\frac{N}{n}} + 2} \left(2 f \sqrt{1-f} e^{-\frac{N}{n}} - f \kappa^2 - 2 e^{-\frac{N}{n}} \sqrt{1-f} \right)}. \quad (83)$$

As before, by using the obtained slow-roll parameters, we can write the scalar spectral index, its running and tensor-to-scalar ratio in terms of the model's parameters and analyze them numerically.

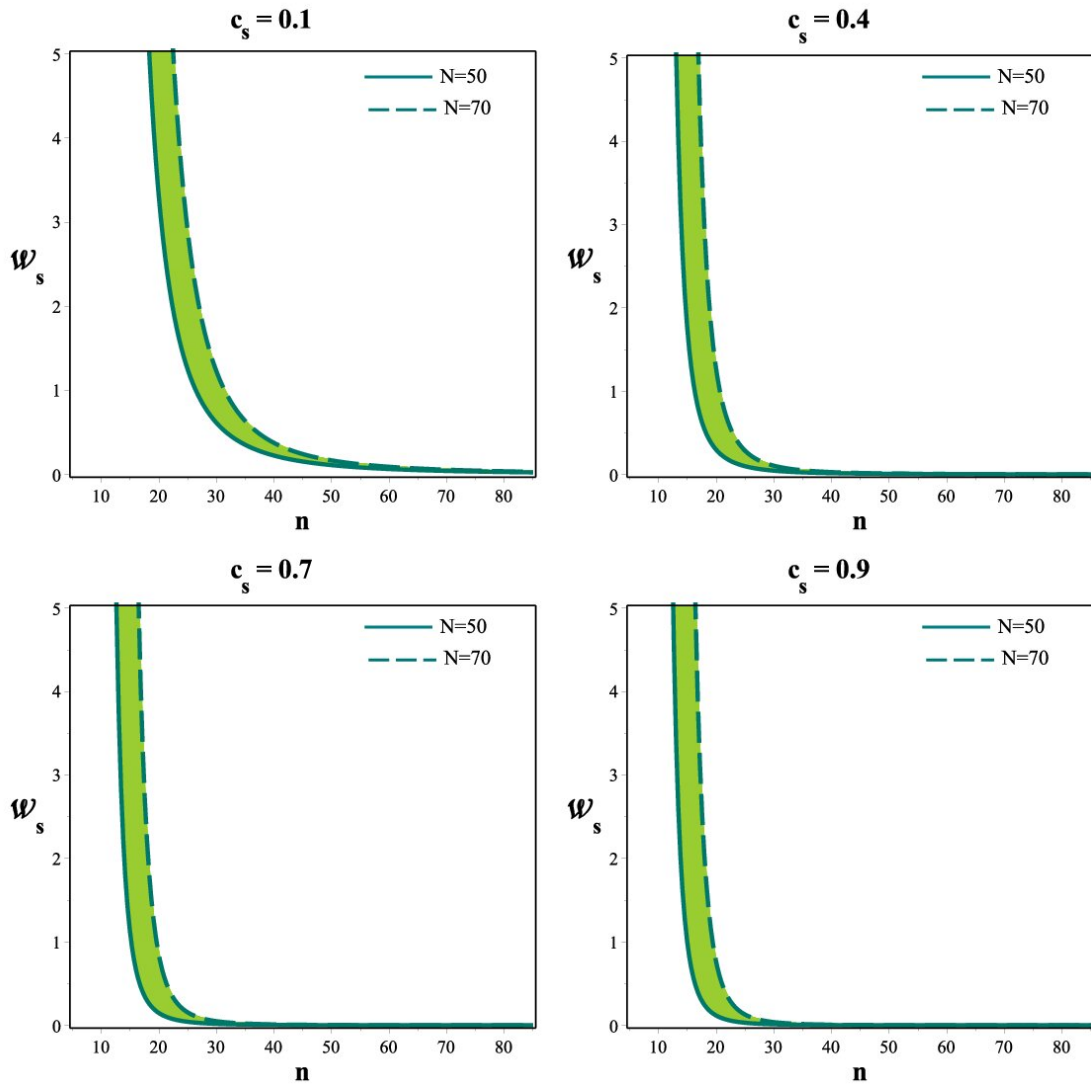


Figure 12: Evolution of \mathcal{W}_s versus n in the domain $50 \leq N \leq 70$ for power-law MDBI inflation with constant sound speed.

In this case, the slow-roll parameters depend on the number of e-folds. Therefore, to obtain the observational constraints we should specify the values of e-fold's number. We adopt three values as $N = 50, 60$ and 70 . Firstly, by using equations (19) and (25) (where the slow-roll parameters are given by equations (81)-(83)), we obtain the parameter space of c_s and n leading to the observationally viable values of $r - n_s$ in the power-law MDBI model. To this end, we have used the Planck2018 TT, TE, EE+lowE+lensing constraints at 68% CL and 95% CL. The results are shown in figure 13, in which the dark magenta region is corresponding to 68% CL and the light magenta region is corresponding to 95% CL of the Planck2018 TT, TE, EE+lowE+lensing data.

Also, to obtain more specific numerical constraints on n and use them in order to explore the running of the scalar spectral index, we study $r - n_s$ plane of the model in the background of Planck2018 TT, TE, EE+lowE+lensing. In this regard, we use the previously adopted values of the sound speed (which are consistent with the constraint obtained from Planck2015 temperature and polarization data). Figure 14 shows the tensor-to-scalar ratio versus the scalar spectral index for power-law MDBI model. By a numerical analysis we have obtained some constraints on n in which $r - n_s$ plane lies within the regions of 68% CL and 95% CL of the Planck2018 TT, TE, EE+lowE+lensing data. These constraints are presented in tables 7 and 8. Here also, by using the obtained constraints on n and observationally viable values of n_s , we explore the running of the scalar spectral index and find the observationally viable values of it. The results are shown in the last column of tables 7 and 8. Also, in figure 15 the evolution of the running of the scalar spectral index versus the scalar spectral index in the background of Planck2018 TT, TE, EE+lowE+lensing dataset is presented. As figure shows, for some values of n , $\alpha_s - n_s$ is consistent with observational data.

Note that the results of the amplitude of the non-Gaussianity are the same for both MDBI and DBI models. This is because for MDBI model also, we use equation (40). Generally, the smaller values of c_s lead to the larger values of f_{NL} . The reason that for the constant sound speed in DBI and MDBI models, the non-Gaussianity is not very large is related to the form of $P(X, \phi)$ for both DBI and MDBI models. In fact, considering that the mimetic constraint is linear in X , allows us to use equation (40) which leads to the observationally viable values of the non-Gaussianity.

At this stage, the difference between the obtained results for a varying sound speed and a constant sound speed needs to be more clarified. In the DBI model with V_+ , the varying sound speed is relatively large, leading to relatively small non-Gaussianity and consistent with observational data. However, in this case the tensor-to-scalar ratio is large and not consistent with observation. So this case is ruled out by observation. In the DBI model with V_- , the varying sound speed is small and the amplitude of the non-Gaussianity is too large to be consistent with the observational data. This case is also ruled out by observation. When we consider the MDBI model, the effect of the mimetic field is that it reduces the value of the tensor-to-scalar ratio. In this regard, $r - n_s$ plane in the MDBI model in some ranges of the parameter n becomes consistent with Planck2018 observational data. For the observationally viable ranges of n , the sound speed is large and the amplitude of the non-Gaussianity is small, which is consistent with observation. For the varying sound speed case, we have considered c_s as a function of the model's parameters. In this regard, the amplitude of the non-Gaussianity also becomes a function of the model's parameters. To constrain c_s and f_{NL} we firstly constrained the parameters of the model in confrontation with observational data. In this regard, we have compared $r - n_s$ values in the MDBI model with Planck2018 data and found some constraints on the parameter n . Since c_s and f_{NL} are functions of n , with obtained constraints on

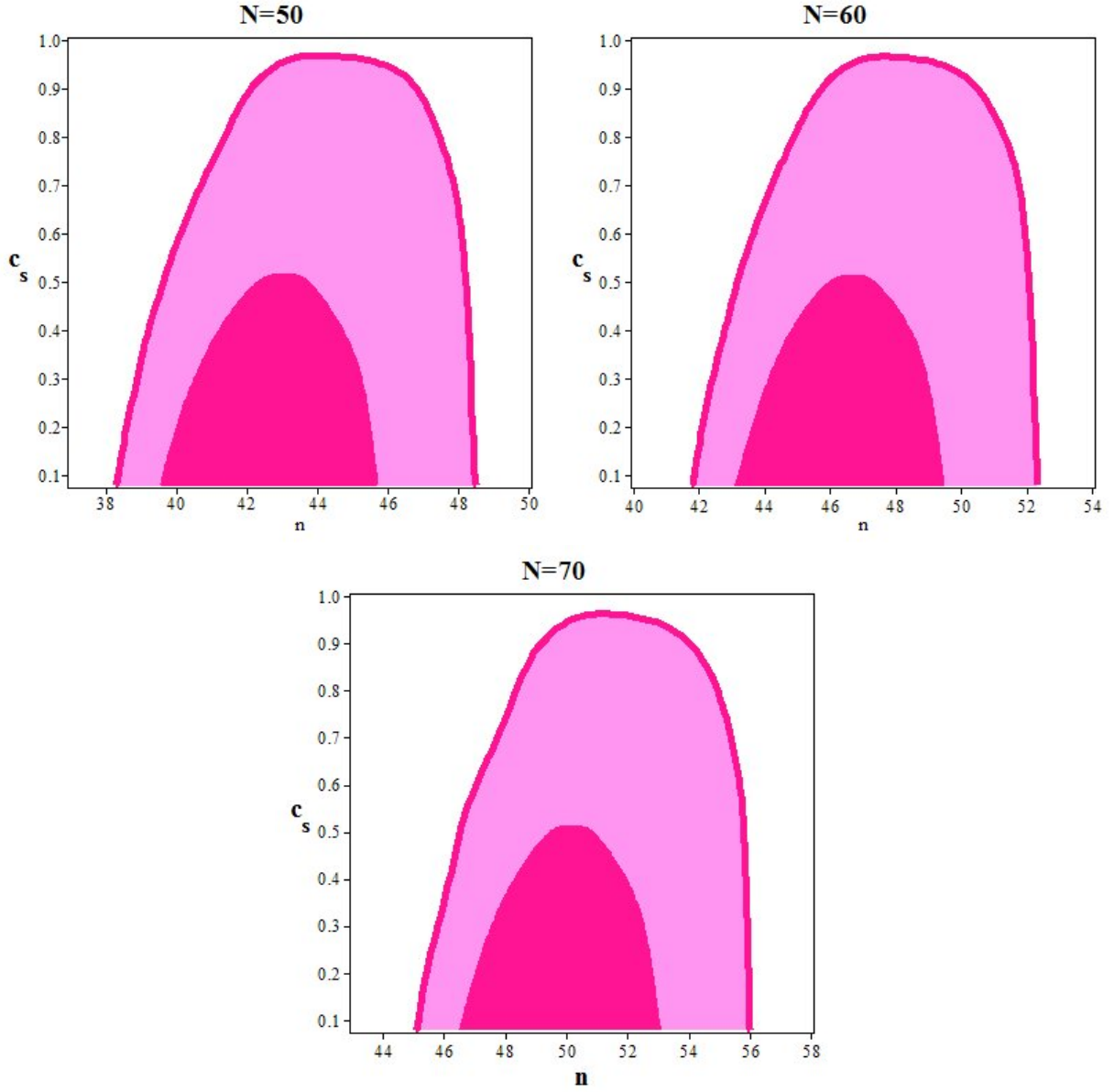


Figure 13: Ranges of parameters c_s and n in which the scalar spectral index and tensor-to-scalar ratio in a power-law MDBI inflation with constant sound speed fulfill the constraints obtained from Planck2018 TT, TE, EE+lowE+lensing at 68% CL (dark magenta region) and 95% CL (light magenta region).

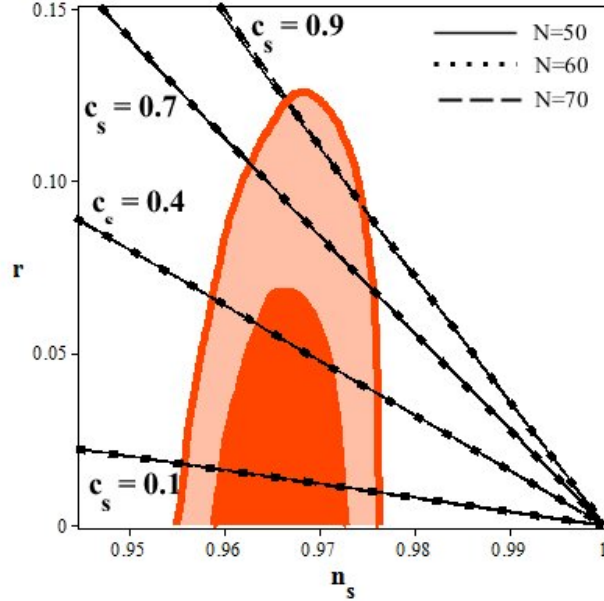


Figure 14: Tensor-to-scalar ratio versus the scalar spectral index for the power-law MDBI inflation with a constant sound speed in the background of Planck2018 TT, TE, EE+lowE+lensing data.

n we were able to constrain the sound speed and the amplitude of the non-Gaussianity in MDBI model.

In the case with a constant sound speed we have considered the sound speed as a free constant parameter. Then the amplitude of the non-Gaussianity would be a constant corresponding to the value of c_s . In this case, both DBI and MDBI models have the same f_{NL} . In the constant sound speed case, we have obtained the potential V and the DBI function f (and also the Lagrange Multiplier λ for the MDBI model) in terms of the sound speed and other model's parameters. Then we have used V , f and λ to obtain the inflation and perturbation parameters such as ϵ , η , s , n_s , α_s and r . We have adopted some sample values of c_s and by probing the observational viability of $r - n_s$, we have found some constraints on the parameter n . Then, we have used the observationally viable ranges of n to obtain the constraints on α_s . Note that the dependence of the potential, DBI function and Lagrange multiplier on c_s is different for the DBI and MDBI models, so the constraints on n and α_s are different in these two models. These are the reasons that why the results in the two sections 2.4 and 3.2 are different.

In summary, our proposed MDBI model with constant sound speed in some ranges of the model's parameter space is ghost-free and consistent with Planck2018 observational data. We shall compare the DBI and MDBI models in details at the end of the paper.

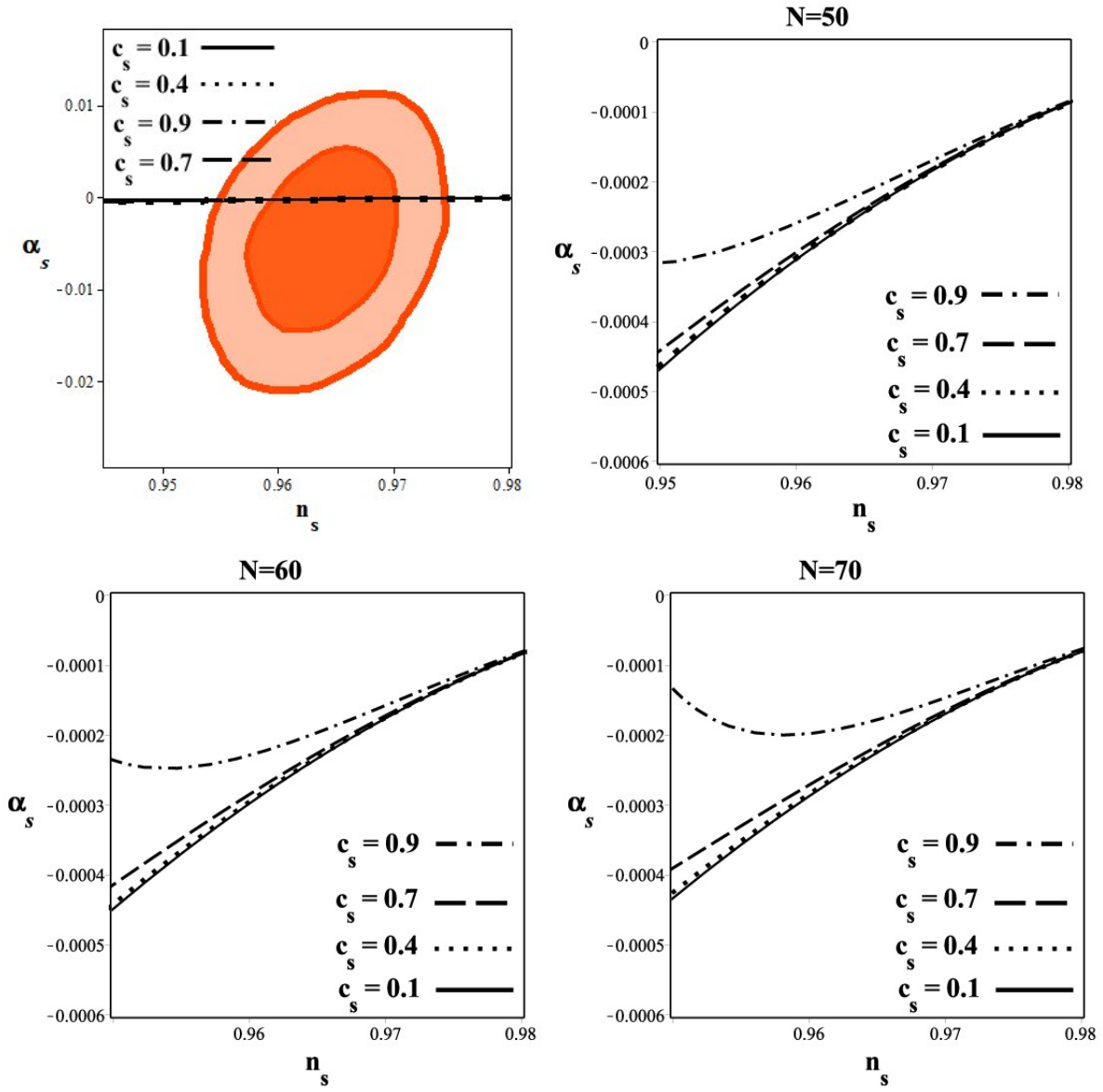


Figure 15: Running of the scalar spectral index versus the scalar spectral index for the power-law MDBI inflation with a constant sound speed in the background of the Planck2018 TT, TE, EE+lowE+lensing data.

Table 7: The ranges of n in which both the scalar spectral index and tensor-to-scalar ratio in the power-law MDBI inflation with constant sound speed are consistent with 95% CL of the Planck2018 TT, TE, EE+lowE+lensing data. This table also shows the constraints on the running of the scalar spectral index obtained from the constraints on n .

| N | c_s | n | α_s |
|-----|-------|---------------------------|--|
| 50 | 0.1 | $38.35 \leq n \leq 48.45$ | $-0.37230 \times 10^{-3} \leq \alpha_s \leq -0.11930 \times 10^{-3}$ |
| 50 | 0.4 | $39.20 \leq n \leq 48.31$ | $-0.32868 \times 10^{-3} \leq \alpha_s \leq -0.12052 \times 10^{-3}$ |
| 50 | 0.7 | $40.7 \leq n \leq 47.9$ | $-0.26408 \times 10^{-3} \leq \alpha_s \leq -0.12353 \times 10^{-3}$ |
| 50 | 0.9 | $42.0 \leq n \leq 46.9$ | $-0.22348 \times 10^{-3} \leq \alpha_s \leq -0.13480 \times 10^{-3}$ |
| 55 | 0.1 | $40.1 \leq n \leq 50.5$ | $-0.36395 \times 10^{-3} \leq \alpha_s \leq -0.11523 \times 10^{-3}$ |
| 55 | 0.4 | $41.1 \leq n \leq 50.3$ | $0.31643 \times 10^{-3} \leq \alpha_s \leq -0.11698 \times 10^{-3}$ |
| 55 | 0.7 | $42.5 \leq n \leq 49.9$ | $-0.25662 \times 10^{-3} \leq \alpha_s \leq -0.11977 \times 10^{-3}$ |
| 55 | 0.9 | $43.8 \leq n \leq 48.8$ | $-0.21779 \times 10^{-3} \leq \alpha_s \leq -0.13161 \times 10^{-3}$ |
| 60 | 0.1 | $41.84 \leq n \leq 52.3$ | $-0.35576 \times 10^{-3} \leq \alpha_s \leq -0.11396 \times 10^{-3}$ |
| 60 | 0.4 | $42.8 \leq n \leq 52.15$ | $-0.31063 \times 10^{-3} \leq \alpha_s \leq -0.11488 \times 10^{-3}$ |
| 60 | 0.7 | $44.2 \leq n \leq 51.8$ | $-0.25180 \times 10^{-3} \leq \alpha_s \leq -0.11689 \times 10^{-3}$ |
| 60 | 0.9 | $45.6 \leq n \leq 50.6$ | $-0.21207 \times 10^{-3} \leq \alpha_s \leq -0.12956 \times 10^{-3}$ |
| 65 | 0.1 | $43.5 \leq n \leq 54.2$ | $-0.34997 \times 10^{-3} \leq \alpha_s \leq -0.11128 \times 10^{-3}$ |
| 65 | 0.4 | $44.5 \leq n \leq 54.0$ | $-0.30429 \times 10^{-3} \leq \alpha_s \leq -0.11265 \times 10^{-3}$ |
| 65 | 0.7 | $46.0 \leq n \leq 53.6$ | $-0.24362 \times 10^{-3} \leq \alpha_s \leq -0.11501 \times 10^{-3}$ |
| 65 | 0.9 | $47.3 \leq n \leq 52.5$ | $-0.20854 \times 10^{-3} \leq \alpha_s \leq -0.12598 \times 10^{-3}$ |
| 70 | 0.1 | $45.15 \leq n \leq 55.95$ | $-0.34392 \times 10^{-3} \leq \alpha_s \leq -0.11006 \times 10^{-3}$ |
| 70 | 0.4 | $46.2 \leq n \leq 55.85$ | $-0.29688 \times 10^{-3} \leq \alpha_s \leq -0.11047 \times 10^{-3}$ |
| 70 | 0.7 | $47.8 \leq n \leq 55.4$ | $-0.23506 \times 10^{-3} \leq \alpha_s \leq -0.11278 \times 10^{-3}$ |
| 70 | 0.9 | $49.0 \leq n \leq 54.2$ | $-0.20467 \times 10^{-3} \leq \alpha_s \leq -0.12484 \times 10^{-3}$ |

Table 8: The ranges of n in which both the scalar spectral index and tensor-to-scalar ratio in the power-law MDBI inflation with constant sound speed are consistent with 68% CL of the Planck2018 TT, TE, EE+lowE+lensing data. This table also shows the constraints on the running of the scalar spectral index obtained from the constraints on n .

| N | c_s | n | α_s |
|-----|-------|---------------------------|--|
| 50 | 0.1 | $39.65 \leq n \leq 45.68$ | $-0.31403 \times 10^{-3} \leq \alpha_s \leq -0.15690 \times 10^{-3}$ |
| 50 | 0.4 | $41.15 \leq n \leq 44.8$ | $-0.25848 \times 10^{-3} \leq \alpha_s \leq -0.17134 \times 10^{-3}$ |
| 50 | 0.7 | not consistent | not consistent |
| 50 | 0.9 | not consistent | not consistent |
| 55 | 0.1 | $41.4 \leq n \leq 47.6$ | $-0.30811 \times 10^{-3} \leq \alpha_s \leq -0.15303 \times 10^{-3}$ |
| 55 | 0.4 | $43.0 \leq n \leq 46.7$ | $-0.25128 \times 10^{-3} \leq \alpha_s \leq -0.16717 \times 10^{-3}$ |
| 55 | 0.7 | not consistent | not consistent |
| 55 | 0.9 | not consistent | not consistent |
| 60 | 0.1 | $43.18 \leq n \leq 49.45$ | $-0.29979 \times 10^{-3} \leq \alpha_s \leq -0.14984 \times 10^{-3}$ |
| 60 | 0.4 | $44.7 \leq n \leq 48.6$ | $-0.24780 \times 10^{-3} \leq \alpha_s \leq -0.16234 \times 10^{-3}$ |
| 60 | 0.7 | not consistent | not consistent |
| 60 | 0.9 | not consistent | not consistent |
| 65 | 0.1 | $44.9 \leq n \leq 51.3$ | $-0.29447 \times 10^{-3} \leq \alpha_s \leq -0.14642 \times 10^{-3}$ |
| 65 | 0.4 | $46.5 \leq n \leq 50.4$ | $-0.24100 \times 10^{-3} \leq \alpha_s \leq -0.15921 \times 10^{-3}$ |
| 65 | 0.7 | not consistent | not consistent |
| 65 | 0.9 | not consistent | not consistent |
| 70 | 0.1 | $46.58 \leq n \leq 53.05$ | $-0.28944 \times 10^{-3} \leq \alpha_s \leq -0.14437 \times 10^{-3}$ |
| 70 | 0.4 | $48.2 \leq n \leq 52.1$ | $-0.23676 \times 10^{-3} \leq \alpha_s \leq -0.15722 \times 10^{-3}$ |
| 70 | 0.7 | not consistent | not consistent |
| 70 | 0.9 | not consistent | not consistent |

4 Confrontation with BICEP2/Keck Array 2014 and Planck2018 data

Planck2018 data are really powerful in constraining the cosmological parameters. However, the constraints on the parameters are somewhat model dependent. For instance, and as we have mentioned in the Introduction, the constraints on the scalar spectral index and tensor-to-scalar ratio, r , are rather different in the Λ CDM+ r and Λ CDM+ $r + \frac{dn_s}{d \ln k}$ models [66]. Especially, when the variation of the scalar spectral index is considered, the upper limit of r is larger [66]. To reduce the degeneracies of the tensor-to-scalar ratio with other cosmological parameters, the Planck2018 team have used the B-mode polarization data from BICEP2/Keck Array 2014 [85]. By using the BICEP/Keck Array-Planck joint cross-correlation, the Planck2018 collaboration have obtained the tighter constraint on the tensor-to-scalar ratio [66]. In this regard, from Planck2018 TT, TE, EE+lowE+lensing+BK14+BAO data, for the Λ CDM+ r model we have [66]

$$r < 0.065 \quad \text{and} \quad n_s = 0.9670 \pm 0.0037 \quad (84)$$

and for Λ CDM+ $r + \frac{dn_s}{d \ln k}$ we have [66]

$$r < 0.072 \quad \text{and} \quad n_s = 0.9658 \pm 0.0038 \quad (85)$$

Our consideration shows that non of the DBI and MDBI models with varying sound speed are consistent with Planck2018 TT, TE, EE+lowE+lensing+BK14+BAO data, however, these models with *constant sound speed* are consistent with the mentioned joint data. We use Planck2018 TT, TE, EE+lowE+lensing+BK14+BAO data at 68% CL and 95% CL to find the the parameter space of c_s and n leading to the observationally viable values of $r - n_s$ in the power-law MDBI model. The results are shown in figure 16.

Here also, we obtain more specific numerical constraints on n and use them to explore the running of the scalar spectral index. In this regard, we study $r - n_s$ plane of the model in the background of Planck2018 TT, TE, EE+lowE+lensing+BK14+BAO data. The adopted values of c_s are the same as the ones in previous section. Figure 17 shows the tensor-to-scalar ratio versus the scalar spectral index for the power-law DBI (left panel) and power-law MDBI (right panel) models. By a numerical analysis we have obtained some constraints on n in which $r - n_s$ plane in these two models lies on the region of 68% CL and 95% CL of the Planck2018 TT, TE, EE+lowE+lensing+BK14+BAO data. These constraints are presented in tables 9-12.

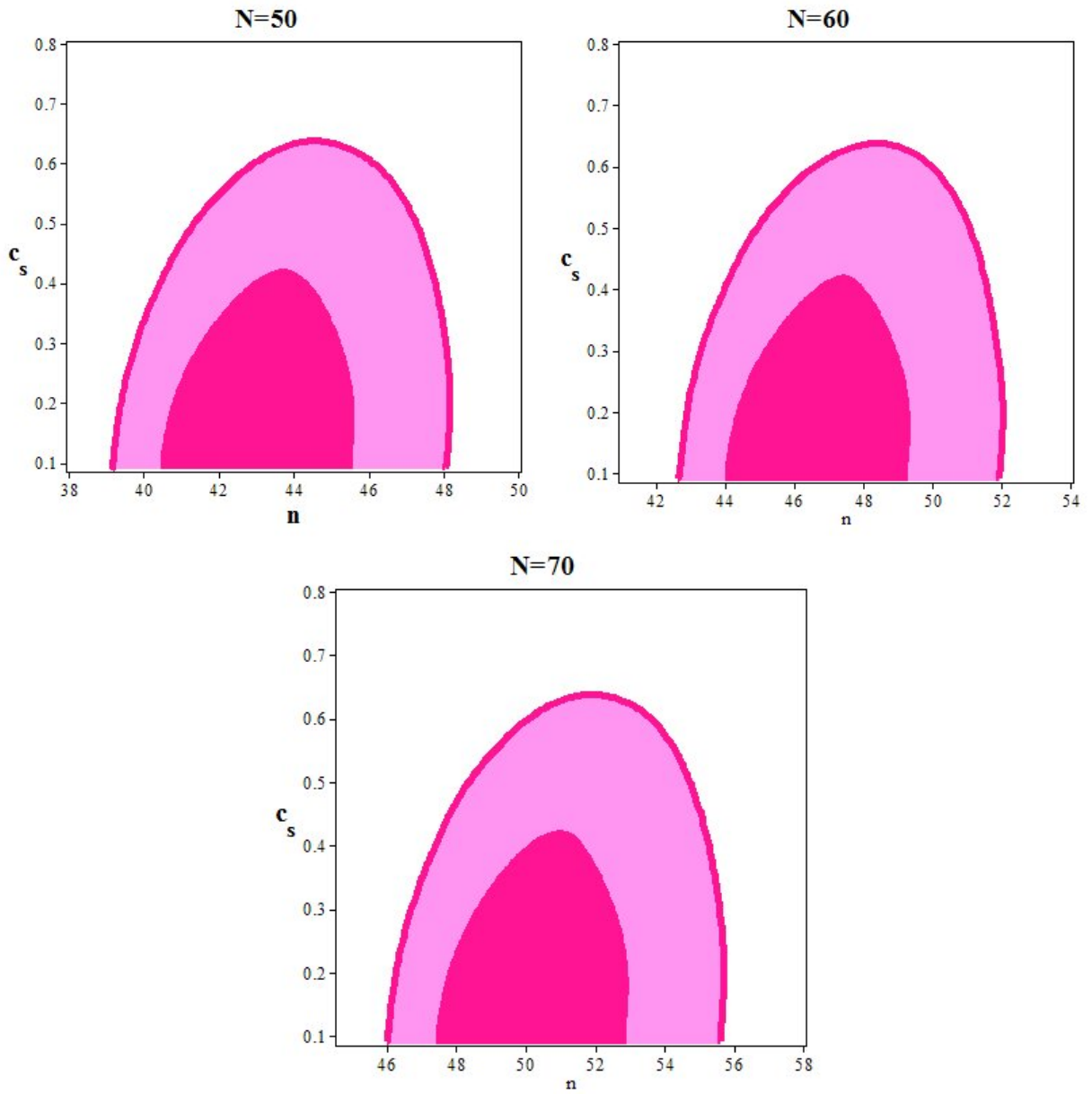


Figure 16: Ranges of parameters c_s and n in which the scalar spectral index and tensor-to-scalar ratio in a power-law MDBI inflation with a constant sound speed fulfill the constraints obtained from Planck2018 TT, TE, EE+lowE+lensing+BK14+BAO at 68% CL (the dark magenta region) and 95% CL (the light magenta region).

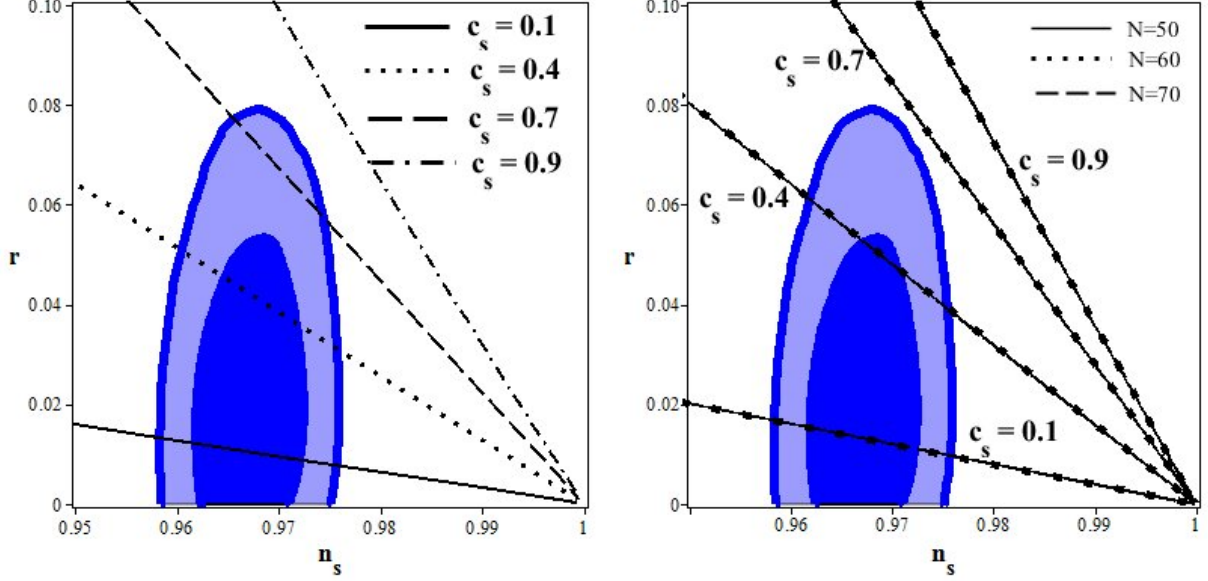


Figure 17: Running of the scalar spectral index versus the scalar spectral index for the power-law DBI inflation (left panel) and power-law MDBI inflation (right panel) with a constant sound speed in the background of the Planck2018 TT, TE, EE+lowE+lensing+BK14+BAO data.

Table 9: The ranges of n in which both the scalar spectral index and tensor-to-scalar ratio in the power-law DBI inflation with a constant sound speed are consistent with 95% CL of the Planck2018 TT, TE, EE+lowE+lensing+BK14+BAO data. This table also shows the constraints on the running of the scalar spectral index obtained from the constraints on n .

| c_s | f_{NL} | n | α_s |
|-------|-----------|----------------------------|--|
| 0.1 | -32.08333 | $119.5 \leq n \leq 205.95$ | $-0.52282 \times 10^{-3} \leq \alpha_s \leq -0.17632 \times 10^{-3}$ |
| 0.4 | -1.70139 | $126.1 \leq n \leq 206$ | $-0.46914 \times 10^{-3} \leq \alpha_s \leq -0.17611 \times 10^{-3}$ |
| 0.7 | -0.33730 | $145.1 \leq n \leq 195$ | $-0.35280 \times 10^{-3} \leq \alpha_s \leq -0.19580 \times 10^{-3}$ |
| 0.9 | -0.07602 | not consistent | not consistent |

Table 10: The ranges of n in which both the scalar spectral index and tensor-to-scalar ratio in the power-law DBI inflation with a constant sound speed are consistent with 68% CL of the Planck2018 TT, TE, EE+lowE+lensing+BK14+BAO data. This table also shows the constraints on the running of the scalar spectral index obtained from the constraints on n .

| c_s | f_{NL} | n | α_s |
|-------|-----------|---------------------------|--|
| 0.1 | -32.08333 | $130.9 \leq n \leq 179.1$ | $-0.43586 \times 10^{-3} \leq \alpha_s \leq -0.23306 \times 10^{-3}$ |
| 0.4 | -1.70139 | $141.3 \leq n \leq 176.8$ | $-0.37381 \times 10^{-3} \leq \alpha_s \leq -0.23897 \times 10^{-3}$ |
| 0.7 | -0.33730 | not consistent | not consistent |
| 0.9 | -0.07602 | not consistent | not consistent |

5 Summary and Conclusion

In the mimetic gravity, to have a non-zero sound speed, one should consider higher order terms as $\gamma \square \phi$ in the action. However, this model suffers from gradient instabilities. By considering the direct couplings of the higher derivatives of the mimetic field to the curvature of the space-time, one can overcome the instabilities issue in some regions of the models' parameters space. In this paper, instead of including the higher order derivatives of the scalar field, we have proposed a new model by adding a DBI like term as $f^{-1} \sqrt{1 - f \dot{\phi}^2}$ in the action of the simple mimetic model with a potential. By adding this term, we can have an instabilities-free mimetic model, at least in some regions of the model's parameters space. Indeed, in this paper, we have considered both the DBI and our newly proposed Mimetic DBI (MDBI) models in details and for the sake of comparison. We have studied the power-law inflation in these models and compared the results with Planck2018 data to seek for the observational viability of the models. In this regard, we have considered two general cases: varying sound speed and constant sound speed. For the case of varying sound speed, by studying $r - n_s$ and $\alpha - n_s$ planes and comparing with Planck2018 observational data, we have found some constraints on the parameter n where $a = a_0 t^n$. The constraints on n gave us the observationally viable values of c_s and f_{NL} . For the constant sound speed, we have used the observationally viable values of f_{NL} to find the viable values of the sound speed. Then, with the viable values of the sound speed, we have found some constraints on n leading to the observationally viable values of r , n_s and α_s .

In the varying sound speed case, we have firstly studied the DBI model. We have obtained the main background equations in this setup. By using these equations, we have obtained the perturbation parameters such as the scalar spectral index, its running and tensor-to-scalar ratio in this setup and also the corresponding potential in terms of the Hubble parameters and its derivatives. By studying the power-law inflation in this model and constructing the corresponding potential, we have shown that this model is not consistent with Planck2018 TT, TE, EE+lowE+lensing data. Note that, although $r - n_s$ plane in this model with V_- is consistent with Planck2018 TT, TE, EE+lowE+lensing data at the 68% CL and 95% CL, but the constraints on n lead to the values of f_{NL} which are too large to be consistent with observational data. Then we have proceeded to see

Table 11: The ranges of n in which both the scalar spectral index and tensor-to-scalar ratio in the power-law MDBI inflation with constant sound speed are consistent with 95% CL of the Planck2018 TT, TE, EE+lowE+lensing+BK14+BAO data. This table also shows the constraints on the running of the scalar spectral index obtained from the constraints on n .

| N | c_s | n | α_s |
|-----|-------|---------------------------|--|
| 50 | 0.1 | $39.16 \leq n \leq 48.08$ | $-0.33491 \times 10^{-3} \leq \alpha_s \leq -0.12342 \times 10^{-3}$ |
| 50 | 0.4 | $40.4 \leq n \leq 47.8$ | $-0.28310 \times 10^{-3} \leq \alpha_s \leq -0.12646 \times 10^{-3}$ |
| 50 | 0.7 | not consistent | not consistent |
| 50 | 0.9 | not consistent | not consistent |
| 55 | 0.1 | $40.90 \leq n \leq 50.0$ | $-0.32817 \times 10^{-3} \leq \alpha_s \leq -0.12076 \times 10^{-3}$ |
| 55 | 0.4 | $42.19 \leq n \leq 49.74$ | $0.27690 \times 10^{-3} \leq \alpha_s \leq -0.12335 \times 10^{-3}$ |
| 55 | 0.7 | not consistent | not consistent |
| 55 | 0.9 | not consistent | not consistent |
| 60 | 0.1 | $42.7 \leq n \leq 51.93$ | $-0.31891 \times 10^{-3} \leq \alpha_s \leq -0.11777 \times 10^{-3}$ |
| 60 | 0.4 | $43.95 \leq n \leq 51.6$ | $-0.27040 \times 10^{-3} \leq \alpha_s \leq -0.12097 \times 10^{-3}$ |
| 60 | 0.7 | not consistent | not consistent |
| 60 | 0.9 | not consistent | not consistent |
| 65 | 0.1 | $44.33 \leq n \leq 53.81$ | $-0.31548 \times 10^{-3} \leq \alpha_s \leq -0.11532 \times 10^{-3}$ |
| 65 | 0.4 | $45.68 \leq n \leq 53.51$ | $-0.26469 \times 10^{-3} \leq \alpha_s \leq -0.11790 \times 10^{-3}$ |
| 65 | 0.7 | not consistent | not consistent |
| 65 | 0.9 | not consistent | not consistent |
| 70 | 0.1 | $46.02 \leq n \leq 55.60$ | $-0.30923 \times 10^{-3} \leq \alpha_s \leq -0.11373 \times 10^{-3}$ |
| 70 | 0.4 | $47.37 \leq n \leq 55.31$ | $-0.25966 \times 10^{-3} \leq \alpha_s \leq -0.11600 \times 10^{-3}$ |
| 70 | 0.7 | not consistent | not consistent |
| 70 | 0.9 | not consistent | not consistent |

Table 12: The ranges of n in which both scalar spectral index and tensor-to-scalar ratio in the power-law MDBI inflation with a constant sound speed are consistent with 68% CL of the Planck2018 TT, TE, EE+lowE+lensing+BK14+BAO data. This table also shows the constraints on the running of the scalar spectral index obtained from the constraints on n .

| N | c_s | n | α_s |
|-----|-------|---------------------------|--|
| 50 | 0.1 | $40.42 \leq n \leq 45.57$ | $-0.28504 \times 10^{-3} \leq \alpha_s \leq -0.15878 \times 10^{-3}$ |
| 50 | 0.4 | $42.7 \leq n \leq 44.51$ | $-0.21590 \times 10^{-3} \leq \alpha_s \leq -0.17677 \times 10^{-3}$ |
| 50 | 0.7 | not consistent | not consistent |
| 50 | 0.9 | not consistent | not consistent |
| 55 | 0.1 | $42.24 \leq n \leq 47.46$ | $-0.27768 \times 10^{-3} \leq \alpha_s \leq -0.15516 \times 10^{-3}$ |
| 55 | 0.4 | $44.58 \leq n \leq 46.37$ | $-0.20992 \times 10^{-3} \leq \alpha_s \leq -0.17298 \times 10^{-3}$ |
| 55 | 0.7 | not consistent | not consistent |
| 55 | 0.9 | not consistent | not consistent |
| 60 | 0.1 | $43.98 \leq n \leq 49.29$ | $-0.27264 \times 10^{-3} \leq \alpha_s \leq -0.15220 \times 10^{-3}$ |
| 60 | 0.4 | $46.4 \leq n \leq 48.2$ | $-0.20487 \times 10^{-3} \leq \alpha_s \leq -0.16918 \times 10^{-3}$ |
| 60 | 0.7 | not consistent | not consistent |
| 60 | 0.9 | not consistent | not consistent |
| 65 | 0.1 | $45.72 \leq n \leq 51.12$ | $-0.26718 \times 10^{-3} \leq \alpha_s \leq -0.14898 \times 10^{-3}$ |
| 65 | 0.4 | $48.15 \leq n \leq 49.98$ | $-0.20101 \times 10^{-3} \leq \alpha_s \leq -0.16596 \times 10^{-3}$ |
| 65 | 0.7 | not consistent | not consistent |
| 65 | 0.9 | not consistent | not consistent |
| 70 | 0.1 | $47.39 \leq n \leq 52.88$ | $-0.26329 \times 10^{-3} \leq \alpha_s \leq -0.14667 \times 10^{-3}$ |
| 70 | 0.4 | $49.84 \leq n \leq 51.79$ | $-0.20052 \times 10^{-3} \leq \alpha_s \leq -0.16368 \times 10^{-3}$ |
| 70 | 0.7 | not consistent | not consistent |
| 70 | 0.9 | not consistent | not consistent |

Table 13: Observational viability of the models considered in this paper.

| Model | Sound Speed | Planck2018 TT, TE, EE+lowE +lensing | Planck2018 TT, TE, EE+lowE +lensing+BK14+BAO |
|-------|-------------|--|---|
| DBI | varying | not consistent | not consistent |
| MDBI | varying | consistent (with $n \sim 10^1$) | not consistent |
| DBI | constant | consistent (with $n \sim 10^2$) | consistent (with $n \sim 10^2$) |
| MDBI | constant | consistent (with $n \sim 10^1$) | consistent (with $n \sim 10^1$) |

the situation in the mimetic DBI scenario.

In the MDBI model, we firstly obtained the main background equations of model. We have also found the Lagrange multiplier and potential in this setup in terms of the Hubble parameter. By numerical studying of the power-law MDBI model, we have shown that this model, in some regions of the model's parameters space, is free of the ghost and gradient instabilities. By obtaining the the perturbation's parameters in this model and comparing the results with the observational data, we have found that our MDBI model is consistent with Planck2018 TT, TE, EE+lowE+lensing data at the 95% CL. In this case, the constraints on n lead to the small amplitude of the non-Gaussianity which is consistent with observation.

In the constant sound speed case also, we have studied both DBI and MDBI inflation with power-law scale factor. We have obtained the potential, the DBI function (f) and the slow-roll parameters in terms of c_s , N and n . We have adopted some sample values of the the sound speed allowed by the Planck2015 data. By these adopted values of the sound speed we have studied $r - n_s$ and $\alpha_s - n_s$ planes numerically and have obtained some constraints on parameter n . Both the DBI and MDBI models with power-law scale factor are consistent with Planck2018 TT, TE, EE+lowE+lensing data at the 68% CL and 95% CL. However, for the DBI model, the constraint on n is as $n \sim 10^2$ while, for the newly proposed MDBI model it is as $n \sim 10^1$. We have also obtained the parameters space of c_s and n in which the scalar spectral index and tensor-to-scalar ratio in a power-law MDBI inflation with constant sound speed fulfill the constraints obtained from Planck2018 TT, TE, EE+lowE+lensing at the 68% CL and 95% CL. According to our analysis, the constraint on the constant sound speed in the power-law MDBI inflation is as $c_s \leq 0.95$.

Finally, we note that to reduce the degeneracies of the tensor-to-scalar ratio with other cosmological parameters and obtain the tighter constraint on the tensor-to-scalar ratio, Planck2018 collaboration has used the B-mode polarization data from BICEP2/Keck Array 2014. In this regard, we have explored the DBI and newly proposed MDBI model in confrontation with Planck2018 TT, TE, EE+lowE +lensing+BK14+BAO data, where BK14 refers to BICEP2/Keck Array 2014 data. The results show that in this case also, the constraint on n for the DBI model is as $n \sim 10^2$ and for the MDBI model it is as $n \sim 10^1$. However, by obtaining the parameters space of c_s and n in which the scalar spectral index and tensor-to-scalar ratio in a power-law MDBI inflation are consistent with Planck2018 TT, TE, EE+lowE+lensing+BK14+BAO at 68% CL and 95% CL, we have found a tighter constraint on the constant sound speed as $c_s \leq 0.64$. Table 13 summarizes

the final results of this paper.

Appendix: The Third Slow-Roll Parameter in the Mimetic DBI (MDBI) Model

$$s = \frac{\sqrt{2} \kappa^5}{4} \left[\frac{54 H^5(N) H''(N) + 162 H'^2(N) H^4(N) + 144 H^4(N) H'(N) H''(N)}{\left(-H'(N) H(N)\right)^{3/2} \left(3 H^2(N) + 2 H(N) H'(N) - \kappa^2\right) J} \right. \\ + \frac{288 H'^3(N) H^3(N) + 120 H^3(N) H'^2(N) H''(N) - 27 H^3(N) H''(N) \kappa^2 + 168 H'^4(N) H^2(N)}{\left(-H'(N) H(N)\right)^{3/2} \left(3 H^2(N) + 2 H(N) H'(N) - \kappa^2\right) J} \\ + \frac{32 H^2(N) H'^3(N) H''(N) + 9 H^2(N) H'^2(N) \kappa^2 - 24 H^2(N) H'(N) H''(N) \kappa^2}{\left(-H'(N) H(N)\right)^{3/2} \left(3 H^2(N) + 2 H(N) H'(N) - \kappa^2\right) J} \\ \left. + \frac{32 H'^5(N) H(N) - 4 H(N) H'^2(N) H''(N) \kappa^2 + 3 H(N) H''(N) \kappa^4 - 4 H'^4(N) \kappa^2 - 3 H'^2(N) \kappa^4}{\left(-H'(N) H(N)\right)^{3/2} \left(3 H^2(N) + 2 H(N) H'(N) - \kappa^2\right) J} \right]$$

with

$$J = 54 H'(N) H^5(N) + 108 H'^2(N) H^4(N) + 72 H'^3(N) H^3(N) - 54 H^3(N) H'(N) \kappa^2 \\ + 16 H'^4(N) H^2(N) - 72 H^2(N) H'^2(N) \kappa^2 - 18 H^2(N) \kappa^4 - 24 H(N) H'^3(N) \kappa^2 \\ - 6 H(N) H'(N) \kappa^4 + 4 H'^2(N) \kappa^4 + 3 \kappa^6$$

Acknowledgement

This work has been supported financially by Research Institute for Astronomy and Astrophysics of Maragha (RIAAM) under research project number 1/6275-6.

References

- [1] A. Chamseddine and V. Mukhanov, JHEP **1311**, 135 (2013).
- [2] A. Golovnev, Phys. Lett. B **728**, 39-40 (2014).
- [3] K. Hammer and A. Vikman, [arXiv:1512.09118].
- [4] A. O. Barvinsky, JCAP **01**, 014 (2014).
- [5] A. Chamseddine and V. Mukhanov, A. Vikman, JCAP **1406**, 017 (2014).
- [6] R. Myrzakulov, L. Sebastiani and S. Vagnozzi, Eur. Phys. J. C **75**, 444 (2015).
- [7] N. Hosseinkhan and K. Nozari, Eur. Phys. J. Plus **133**, 50 (2018).
- [8] N. Sadeghnezhad and K. Nozari, Phys. Lett. B **769**, 134 (2017).

- [9] S. Nojiri and S. D. Odintsov, *Mod. Phys. Lett. A* **29**, 1450211 (2014).
- [10] A. V. Astashenok and S. D. Odintsov, *Phys. Rev. D* **94**, 063008 (2016).
- [11] S. Nojiri, S. D. Odintsov and V. K. Oikonomou, *Phys. Rev. D* **94**, 104050 (2016).
- [12] A. V. Astashenok, S. D. Odintsov and V. K. Oikonomou, *Class. Quant. Grav.* **32**, 185007 (2015).
- [13] G. Cognola *et al.*, *Class. Quant. Grav.* **33**, 225014 (2016).
- [14] F. Arroja *et al.*, *JCAP* **1509**, 051 (2015).
- [15] Z. Haghani *et al.*, [arXiv:1404.7689].
- [16] S. D. Odintsov and V. K. Oikonomou, *Astrophys. Space Sci.* **361**, 174 (2016).
- [17] M. Bouhmadi-Lopez, C. -Y. Chen and P. Chen, *JCAP* **11**, 053 (2017).
- [18] C. -Y. Chen, M. Bouhmadi-Lopez and P. Chen, *Eur. Phys. J. C* **78**, 59 (2018).
- [19] A. Ijjas, J. Ripley and P. J. Steinhardt, *Phys. Lett. B* **760**, 132, (2016).
- [20] Y. Zheng, L. Shen, Y. Mou and M. Li, *JCAP* **08**, 040 (2017).
- [21] F. Capela and S. Ramazanov, *JCAP* **1504**, 051 (2015).
- [22] L. Mirzaghali and A. Vikman, *JCAP* **1506**, 028 (2015).
- [23] O. Malaeb, *Phys. Rev. D* **91**, 103526 (2015).
- [24] S. Ramazanov, *JCAP* **1512**, 007 (2015).
- [25] D. Langlois and K. Noui, *JCAP* **1607**, 016 (2016).
- [26] S. Ramazanov *et al.*, *JHEP* **06**, 020 (2016).
- [27] F. Arroja *et al.*, *JCAP* **1604**, 042 (2016).
- [28] J. Ben Achour, D. Langlois and K. Noui, *Phys. Rev. D* **93**, 124005 (2016).
- [29] S. Hirano, S. Nishi and T. Kobayashi, *JCAP* **1707**, 009 (2017).
- [30] Y. Cai and Y. -S. Piao, *Phys. Rev. D* **96**, 124028 (2017).
- [31] K. Takahashi and T. Kobayashi, *JCAP* **11**, 038 (2017).
- [32] D. Yoshida *et al.*, *Phys. Rev. D* **96**, 043502 (2017).
- [33] E. Silverstein and D. Tong, *Phys. Rev. D* **70**, 103505 (2004).
- [34] X. Chen *et al.*, *JCAP* **0701**, 002 (2007).
- [35] M. Alishahiha, E. Silverstein, and D. Tong, *Phys. Rev. D* **70**, 123505 (2004).

- [36] X. Chen, J. High Energy Phys. **0508**, 045 (2005).
- [37] A. Sen, J. High Energy Phys. **10**, 008 (1999).
- [38] A. Sen, J. High Energy Phys. **07**, 065 (2002).
- [39] A. Sen, Mod. Phys. Lett. A **17**, 1797 (2002).
- [40] K. Nozari and N. Rashidi, Phys. Rev. D **88**, 023519 (2013).
- [41] K. Nozari and N. Rashidi, Phys. Rev. D **90**, 043522 (2014).
- [42] N. Rashidi, K. Nozari and Ø. Grøn, JCAP **05**, 044 (2018).
- [43] M. Li, T. Wang, and Y. Wang, JCAP **03**, 028 (2008)
- [44] X. Chen, Phys. Rev. D **72**, 123518 (2005).
- [45] M. Spalinski, JCAP **0705**, 017 (2007).
- [46] K. Nozari and N. Rashidi, Phys. Rev. D **88**, 084040 (2013).
- [47] S. Li and A. R Liddle, JCAP **03**, 044 (2014).
- [48] N. Nazavari *et al.*, Phys. Rev. D **93**, 123504 (2016).
- [49] T. Qiu, Phys. Rev. D **93**, 123515 (2016).
- [50] K. S. Kumar *et al.*, JCAP **02**, 063 (2016).
- [51] S. Choudhury and S. Pal, Eur. Phys. J. C **75**, 241 (2015).
- [52] N. Rashidi, K. Nozari, Int. J. Mod. Phys. D **27**, 1850076 (2018).
- [53] J. Chen *et al.*, Chinese Physics C **42**, 045102 (2018).
- [54] R. Amani, K. Rezazadeh, A. Abdolmaleki and K. Karami, The Astrophysical Journal **853**, 188 (2018).
- [55] S. Rasouli, K. Rezazadeh, K. Karami and A. Abdolmaleki, [arXiv:1807.05732].
- [56] F. Lucchin and S. Matarrese, Phys. Rev. D **32**, 1316 (1985).
- [57] J. Halliwell, Phys. Lett. B **185**, 341 (1987).
- [58] A. R. Liddle, Phys. Lett. B **220**, 502 (1989).
- [59] M. Spalinski, Phys. Lett. B **650**, 313 (2007).
- [60] S. Unnikrishnan and V. Sahni, JCAP **10**, 063 (2013).
- [61] K. Bamba, S. Nojiri, S. D. Odintsov and D. Sáez-Gómez, Phys. Rev. D **90**, 124061 (2014).
- [62] S. D. Odintsov and V. K. Oikonomou, Annals of Physics **363**, 503 (2015).

- [63] E. Ellis *et al.*, Gen. Relativ. Gravit. **39**, 1651 (2007).
- [64] I. Quiros *et al.*, Class. Quantum Grav. **35**, 075005 (2018), DOI:10.1088/1361-6382/aaae24.
- [65] N. Aghanim *et al.*, [arXiv:1807.06209].
- [66] Y. Akrami *et al.*, [arXiv:1807.06211].
- [67] M. Kamionkowski *et al.*, Phys. Rev. D **55**, 7368 (1997).
- [68] M. Zaldarriaga and U. Seljak, Phys. Rev. D **55**, 1830 (1997).
- [69] U. Seljak and M. Zaldarriaga, Phys. Rev. Lett. **78**, 2054 (1997).
- [70] W. Hu and M. J. White, Phys. Rev. D **56**, 596 (1997).
- [71] W. Hu *et al.*, Phys. Rev. D **57**, 3290 (1998).
- [72] U. Seljak and M. Zaldarriaga, The Astrophysical Journal **469**, 437 (1996).
- [73] A. Lewis, A. Challinor, and A. Lasenby, The Astrophysical Journal **538**, 473 (2000).
- [74] P. A. R. Ade *et al.*, Astron. Astrophys. **594**, A20 (2016).
- [75] J. Lesgourgues, CERN-PH-TH/2011-081, LAPTH-009/11 [arXiv:1104.2932].
- [76] D. Blaset *et al.*, JCAP **1107**, 034 (2011).
- [77] J. Adams *et al.*, Phys. Rev. D **64**, 123514 (2001).
- [78] G. Simard, D. Hanson and G. Holder, The Astrophysical Journal **807**, 166 (2015).
- [79] H. V. Peiris *et al.*, The Astrophysical Journal **148**, 213 (2003).
- [80] G. Simard *et al.*, The Astrophysical Journal **807**, 166 (2015).
- [81] A. De Felice and S. Tsujikawa, Phys. Rev. D **84**, 083504 (2011).
- [82] A. De Felice and S. Tsujikawa, JCAP **1104**, 029 (2011).
- [83] K. Nozari and N. Rashidi, Phys. Rev. D **95**, 123518 (2017).
- [84] J. M. Maldacena, J. High Energy Phys. **05**, 013 (2003).
- [85] P. A. R. Ade *et al.*, Phys. Rev. Lett. **116**, 031302 (2016).
- [86] K. Nozari and N. Rashidi, The Astrophysical Journal **863**, 133 (2018).